Self-consistent model of magnetospheric ring current and propagating electromagnetic ion cyclotron waves: Waves in multi-ion magnetosphere

G. V. Khazanov,[1] K. V. Gamayunov,[1] D. L. Gallagher,[1] and J. U. Kozyra[2]

Received 5 May 2006; revised 19 June 2006; accepted 7 July 2006; published 5 October 2006.

[1] The further development of a self-consistent theoretical model of interacting ring current ions and electromagnetic ion cyclotron waves (Khazanov et al., 2003) is presented. In order to adequately take into account wave propagation and refraction in a multi-ion magnetosphere, we explicitly include the ray tracing equations in our previous self-consistent model and use the general form of the wave kinetic equation. This is a major new feature of the present model and, to the best of our knowledge, the ray tracing equations for the first time are explicitly employed on a global magnetospheric scale in order to self-consistently simulate the spatial, temporal, and spectral evolution of the ring current and of electromagnetic ion cyclotron waves. To demonstrate the effects of EMIC wave propagation and refraction on the wave energy distribution and evolution, we simulate the May 1998 storm. The main findings of our simulation can be summarized as follows. First, owing to the density gradient at the plasmapause, the net wave refraction is suppressed, and He^+-mode grows preferably at the plasmapause. This result is in total agreement with previous ray tracing studies and is very clearly found in presented B field spectrograms. Second, comparison of global wave distributions with the results from another ring current model (Kozyra et al., 1997) reveals that this new model provides more intense and more highly plasmapause-organized wave distributions during the May 1998 storm period. Finally, it is found that He^+-mode energy distributions are not Gaussian distributions and most important that wave energy can occupy not only the region of generation, i.e., the region of small wave normal angles, but all wave normal angles, including those to near 90°. The latter is extremely crucial for energy transfer to thermal plasmaspheric electrons by resonant Landau damping and subsequent downward heat transport and excitation of stable auroral red arcs.

Citation: Khazanov, G. V., K. V. Gamayunov, D. L. Gallagher, and J. U. Kozyra (2006), Self-consistent model of magnetospheric ring current and propagating electromagnetic ion cyclotron waves: Waves in multi-ion magnetosphere, *J. Geophys. Res.*, *111*, A10202, doi:10.1029/2006JA011833.

1. Introduction

[2] The effect of electromagnetic ion cyclotron (EMIC) waves on the Earth's ring current (RC) dynamics is one of the best known examples of wave-particle interaction, and at the same time it is the most controversial mechanism of RC loss [*Walt and Voss*, 2001, 2004]. As a rule, the effective temperatures of RC ions transverse to, $T_\perp$, and along, $T_\parallel$, geomagnetic field line comply with an inequality $T_\perp > T_\parallel$. If an ion temperature anisotropy, $A = T_\perp/T_\parallel - 1$, exceeds some positive threshold, EMIC waves could be generated [*Cornwall*, 1964, 1965; *Kennel and Petschek*, 1966]. These waves have been observed in the inner [e.g., *LaBelle et al.*, 1988; *Erlandson and Ukhorskiy*, 2001] and outer [*Anderson et al.*, 1992a, 1992b] magnetosphere, at geostationary orbit [*Young et al.*, 1981; *Mauk*, 1982], at high latitudes along the plasmapause [*Erlandson et al.*, 1990], and at ionospheric altitudes [*Iyemori and Hayashi*, 1989; *Bräysy et al.*, 1998]. Measurements taken on board the GEOS 1 and 2 satellites have revealed a critical role of the thermal He^+ admixture for generation and propagation of EMIC waves [*Young et al.*, 1981; *Roux et al.*, 1982]. These observations have stimulated theoretical studies in which the influence of a thermal He^+ admixture on EMIC waves has been considered [*Mauk*, 1982; *Roux et al.*, 1982; *Gomberoff and Neira*, 1983; *Gendrin et al.*, 1984; *Denton et al.*, 1992]. The effects of energetic RC heavy ions (He^+ and O^+) on the generation of EMIC waves in a multi-ion core plasma (H^+, He^+, O^+) have been studied by *Kozyra et al.* [1984].

[3] The RC-EMIC wave interaction causes scattering of ions into the loss cone and leads to decay of the RC [e.g., *Cornwall et al.*, 1970], especially during the main phase of storms when the RC decay times of about 1 hour or less are

[1]Space Science Department, National Space Science and Technology Center, NASA Marshall Space Flight Center, Huntsville, Alabama, USA.
[2]Space Physics Research Laboratory, University of Michigan, Ann Arbor, Michigan, USA.

0148-0227/06/2006JA011833

possible [*Gonzalez et al.*, 1989]. Obliquely propagating EMIC waves are damped due to Landau resonance with thermal plasmaspheric electrons, and subsequent transport of the dissipating wave energy into the ionosphere causes an ionosphere temperature enhancement. This process has been employed by *Cornwall et al.* [1971] as a major physical mechanism which is able to drive stable auroral red arc emissions during the recovery phase of a storm. Measurements taken aboard the Prognoz satellites have revealed a so-called hot zone near the plasmapause where the temperature of core plasma ions can reach tens of thousands of degrees [*Bezrukikh and Gringauz*, 1976; *Gringauz*, 1983, 1985]. In order to explain this temperature enhancement *Galeev* [1975] has suggested to take into account the induced scattering of EMIC waves by plasmaspheric protons. This nonlinear wave-particle interaction process has been successfully employed later in a plasmasphere-RC interaction model by *Gorbachev et al.* [1992]. Relativistic electrons in the outer radiation belt also interact well with EMIC waves. During magnetic storms, electrons with energy $\geq$1 MeV can be removed by EMIC waves over a timescale of several hours to a day [*Summers and Thorne*, 2003].

[4] *Jordanova et al.* [1997, 1998b, 2001] developed a kinetic model of the terrestrial RC, and for the first time included a quasi-linear RC-EMIC wave interaction on a global scale. The effect of wave-particle interaction on the RC distributions was included in the model by using diffusion coefficients which were obtained for the case of a multi-ion plasmaspheric thermal plasma [*Jordanova et al.*, 1996b]. In that model the hot plasma dispersion relation of EMIC waves was employed [*Kozyra et al.*, 1984] and solved together with the RC bounce-averaged kinetic equations. Number densities, parallel and perpendicular temperatures, and temperature anisotropies of the RC H^+, O^+, and He^+ ions were obtained by taking the moments of the phase space distribution functions, and were then used to calculate the wave growth rates of EMIC waves in bi-Maxwellian plasmas. In order to obtain the gain of EMIC waves, G, the equatorial field-aligned growth rates were then integrated along wave paths, which are field-aligned. *Jordanova et al.* [2001], using the fit $B_w = B_{sat}\ 10^{(G-G_{max})/G_{min}}$, related a calculated wave gain with the measured EMIC wave amplitudes on the basis of a statistical study. The saturation value B_{sat} = 10 nT was obtained from observations [*Anderson et al.*, 1992a, 1992b; *Bräysy et al.*, 1998], where G_{min}, G_{max} are 20 and 60 dB, respectively, i.e., the range 0.1–10 nT for B_w was adopted.

[5] While valuable information can be obtained using a semiempirical approach such as that used by *Jordanova et al.* [2001], it is well-known that the effects of EMIC waves on RC dynamics (and back RC on EMIC waves) strongly depend on such particle/wave characteristics as the ion phase space distribution function, frequency, wave normal angle, wave polarization, wave energy, and form of the wave power spectral density. All these characteristics cannot be independent and should ideally be self-consistently determined by evolution of the wave-ion system itself. In order to properly quantify the EMIC wave and the RC ion dynamics, *Khazanov et al.* [2002, 2003] developed a self-consistent theoretical model of the RC ions and EMIC waves. This model assumes that EMIC waves propagate along geomagnetic field lines, and neglects wave refraction. *Horne and Thorne* [1993] used the "HOTRAY" ray tracing program in order to study the role of propagation and refraction in the generation of different branches of EMIC waves in multi-ion thermal plasma. They found that the local growth rate alone can not determine the resulting wave amplification, and propagation effects have a major impact on the path-integrated wave gain. Recently, *Loto'aniu et al.* [2005] used magnetic and electric field data from the Combined Release and Radiation Effects Satellite (CRRES) in order to obtain the Poynting vector for Pc-1 EMIC waves. They found bidirectional wave energy propagation both away and toward the equator for events observed below 11° MLat and unidirectional energy propagation away from the equator for all events outside 11° of the equator. *Engebretson et al.* [2005] found a similar EMIC wave energy propagation dependence with mixed direction within approximately ±20° MLat and consistently toward the ionosphere for higher magnetic latitudes. These observations allow *Engebretson et al.* [2006] to state that "the mixed directions observed in the above studies near the equator is evidence of wave reflection at the off-equatorial magnetic latitude corresponding to the ion–ion hybrid frequency. Waves that reflect would then set up a standing (bidirectional) pattern in the equatorial magnetosphere. Waves that tunnel through would tend to be absorbed in the ionosphere and not be able to return to equatorial latitudes." So we are consequently required to generalize our previous self-consistent RC-EMIC wave model [*Khazanov et al.*, 2003] in order to adequately take into account the effects of wave propagation, refraction, and reflection in multispecies plasma.

[6] The present study further develops a self-consistent theoretical model of RC ions and EMIC waves [*Khazanov et al.*, 2002, 2003], where we explicitly incorporate into the model the effects of wave propagation and refraction in multi-ion magnetospheric plasma. This article, paper 1, is organized as follows. In section 2 we present a ray tracing model for EMIC waves and compare the results of ray tracing simulations with previously published results. In section 3 we derive a bounce-averaged kinetic equation for He^+-mode of EMIC waves in frequency range $\Omega_{O^+} < \omega < \Omega_{He^+}$. We also quantify and discuss the tunnelling of EMIC waves across the reflection region in multi-ion plasma. The new system of governing equations is summarized in section 4, along with the approaches and initial/boundary conditions used in a subsequent simulation. The patterns of global and spectral distributions for the He^+-mode of EMIC waves during the May 1998 storm period are presented and analyzed in section 5. In the same section, we compare the presented global wave distributions with the results from another global model where a different EMIC wave description has been adopted [*Kozyra et al.*, 1997]. Section 6 summarizes the main features of the developed model and the findings of paper 1.

[7] Paper 2 will continue presentation and discussion of the initial results from this new model, where we will focus on wave induced RC ion precipitation and energy transfer to thermal plasmaspheric electrons by resonant Landau damping of propagating EMIC waves.

2. Ray Tracing Model: Differential Equations and Numerical Algorithm

[8] The general set of ray tracing equations (the so-called approximation of "geometric optics") is well-known and

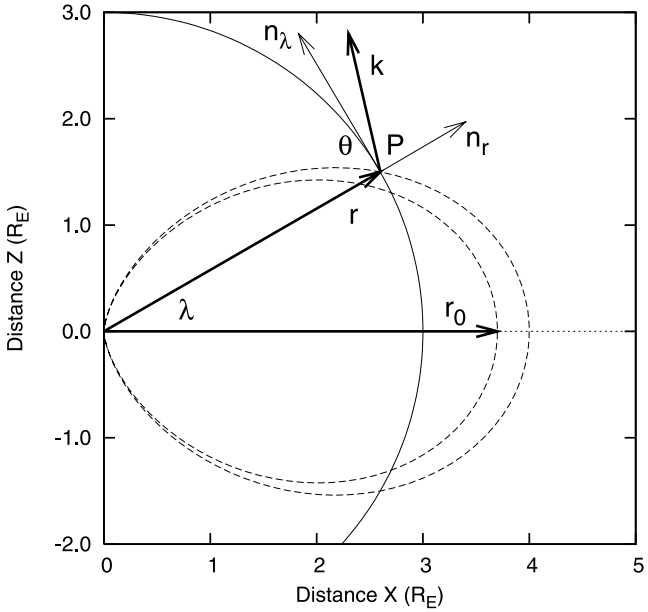

Figure 1. The coordinate systems used to integrate ray tracing equations is shown. In the Earth-centered polar coordinate system any point P, which lies on the raypath, is characterized by length of the radius vector, r, and magnetic latitude, λ. The wave vector $\mathbf{k}$ has components k_r and k_λ in a local Cartesian coordinate system centered on the point P with its unit vector $\mathbf{n_r}$ and $\mathbf{n_\lambda}$ oriented as shown. The θ is the angle between the direction of the local magnetic field and wave normal vector orientation. The r_0 is an equatorial coordinate of the raypath, and dash lines are two dipole magnetic field lines which cross P, and the equatorial points on the ray path.

may be found in many plasma physics monographs [see, e.g., *Stix*, 1992]. These equations were originally derived by *Haselgrove* [1954] and *Haselgrove and Haselgrove* [1960] by employing the method of Hamilton and have subsequently been widely used [e.g., *Yabroff*, 1961; *Kimura*, 1966; *Rauch and Roux*, 1982; *Horne*, 1989]. In the present study, in order to solve the ray tracing equations, we employ a dipole approximation for a geomagnetic field, and in spite of our MLT-dependent plasma density model we ignore a slight longitudinal drift of the waves during propagation [see, e.g., *Bespalov and Trakhtengerts*, 1986]. Under these assumptions the complete three-dimensional (3-D) ray tracing equation set is reduced to a plane geometry. To write down these equations and carry out their subsequent integration, we use two coordinate systems as shown in Figure 1. The Earth-centered polar coordinate system is used to characterize any point P, which lies on the ray trajectory by length of the radius vector, r, and magnetic latitude, λ. The wave vector $\mathbf{k}$ is described by two components, k_r and k_λ, in a local Cartesian coordinate system centered on the current point P, and with its axes oriented along the radius vector and the magnetic latitude direction, respectively (see Figure 1). Using the selected coordinate systems and assuming the medium is stationary (in other words, the characteristic changing timescale for the plasmaspheric thermal plasma is much greater then the characteristic wave propagation time), the resulting system of ray tracing equations can be written as (compare to *Haselgrove* [1954], *Haselgrove and Haselgrove* [1960], *Yabroff* [1961], *Kimura* [1966], and *Burtis* [1973])

$$\frac{dr}{dt} = -\frac{\left(\frac{\partial G}{\partial \mathbf{k}}\right)_r}{\frac{\partial G}{\partial \omega}} \equiv v_{g,r}, \tag{1}$$

$$\frac{d\lambda}{dt} = -\frac{\left(\frac{\partial G}{\partial \mathbf{k}}\right)_\lambda}{\frac{\partial G}{\partial \omega}} \equiv v_{g,\lambda}, \tag{2}$$

$$\frac{dk_r}{dt} = k_\lambda \frac{d\lambda}{dt} + \frac{\left(\frac{\partial G}{\partial \mathbf{r}}\right)_r}{\frac{\partial G}{\partial \omega}}, \tag{3}$$

$$\frac{dk_\lambda}{dt} = -\frac{k_\lambda}{r}\frac{dr}{dt} + \frac{\left(\frac{\partial G}{\partial \mathbf{r}}\right)_\lambda}{\frac{\partial G}{\partial \omega}}. \tag{4}$$

In these equations the following notations are introduced: t is the group time, ω is the angular wave frequency, $v_{g,r} \equiv v_{g,r}(\mathbf{k}, \mathbf{r})$ and $v_{g,\lambda} \equiv v_{g,\lambda}(\mathbf{k}, \mathbf{r})$ are the components of wave group velocity parallel to radius vector and to magnetic latitude direction, respectively, $G \equiv G(\omega, \mathbf{k}, \mathbf{r})$ is a function which only has roots for EMIC eigenmodes, i.e., $G = 0$ at any point along EMIC wave phase trajectories. In this study we use the following form for the function G:

$$G = \left(\frac{kc}{\omega}\right)^2 - N^2(\omega, \mathbf{k}, \mathbf{r}), \tag{5}$$

where N is the refractive index of the EMIC wave modes. Since the main dispersion effects for EMIC waves can be described in the cold plasma approximation, the differences between the raypaths for hot and cold plasmas should be minor (this was also stated by *Horne and Thorne* [1993] after performing ray tracing simulations). This fact allows us to use the cold plasma approximation in order to derive the refractive index N, and its general expression can be found, e.g., in the work of *Stix* [1992] and *Lyons and Williams* [1984]. In spite of the fact that all RC ions (mainly H^+, O^+, and He^+ ions) are "hot," the major EMIC wave dispersion properties can still be described by the cold plasma approximation (of course we are talking here about the real part of N). So the "cold" refractive index depends on the influence of both the thermal and RC plasmas. In order to calculate this refractive index we assume that the core plasmaspheric plasma consists not only of H^+ ions but also of He^+ and O^+ ions. The employed thermal plasma density models will be described below.

[9] The system of Hamilton's equations (1) –(4) including the dispersion relation (5) are integrated using the Adams predictor-corrector method which has been previously employed in many ray tracing simulations [e.g., *Yabroff*, 1961; *Kimura*, 1966; *Burtis*, 1973; *Rauch and Roux*, 1982; *Horne*, 1989]. In this method the length of integration step Δt, is automatically adjusted in order to keep the desired tolerance between predicted and corrected values. Usually, we set $e_{rel} = 10^{-5}$ as the relative error for all variables, and $e_{abs} = 10^{-4}$ degrees as the absolute error for calculation of latitude, but we also prevent Δt from being greater than $\tau \approx 10^{-2}$ seconds during integration. In each

τ seconds, substituting the results of integration in local dispersion relation (5), we calculate the wave frequency, ω_τ. If the relative error is big enough, namely $|\omega_\tau - \omega|/\omega > 5 \cdot e_{rel}$, then the wave number, k, found from integration is corrected as suggested by *Yabroff* [1961].

[10] In order to test and verify our ray tracing code, we set out to reproduce the previously published results for EMIC wave propagation in a multicomponent plasma. The side by side comparisons of our results with the previous ray tracing studies are presented in Appendix A for different density models and for all possible EMIC wave modes. Overall, we find very good agreement between the results, and we believe that our ray tracing code is validated.

3. Wave Kinetic Equation

[11] In order to model EMIC wave dynamics, *Khazanov et al.* [2002, 2003] employed the bounce-average wave kinetic equation that only describes waves propagating along geomagnetic field lines and neglects wave refraction (see equation (2) in these papers). These assumptions can not always be true, and as we showed in Appendix A, propagating EMIC waves easily become highly oblique and deflect from the magnetic field line. In this section we derive the bounce-average wave kinetic equation that takes into account these effects.

3.1. Bounce-Averaged Equation and Its Solution

[12] In order to obtain the equation that describes EMIC wave energy evolution, let us start from the wave kinetic equation [e.g., *Stix*, 1992]. If the background medium is stationary (in other words, the characteristic timescale for the changing of plasmaspheric thermal plasma is much greater then the wave energy evolution time), this equation has the form of

$$\frac{\partial W(\mathbf{r},t,\mathbf{k})}{\partial t} + \frac{\partial \omega(\mathbf{r},\mathbf{k})}{\partial \mathbf{k}} \cdot \frac{\partial W}{\partial \mathbf{r}} - \frac{\partial \omega}{\partial \mathbf{r}} \cdot \frac{\partial W}{\partial \mathbf{k}} = 2\gamma(\mathbf{r},t,\mathbf{k}) \cdot W. \quad (6)$$

In this equation $W(\mathbf{r}, t, \mathbf{k})$ is the EMIC wave power spectral density, and $\gamma(\mathbf{r}, t, \mathbf{k})$ includes both the energy source due to wave interaction with RC ions and the energy sink due to absorption by thermal and hot plasmas. Note that in spite of the quasi-stationarity of the background plasma, the RC itself can vary. In practice it cannot change the dispersive properties of the medium, but may lead to modification of γ, and we specify this explicit time dependence in γ. As we can see, characteristics of the left-hand side of equation (6) are solutions of the ray tracing equations (1)–(4), and $W(\mathbf{r}, t, \mathbf{k})$ is just transferred along the corresponding ray phase trajectories with simultaneous growth/damping depending on the sign of γ along these trajectories.

[13] In an $e - H^+ - He^+ - O^+$ plasma, if EMIC wave generation is caused by the hot RC protons with positive temperature anisotropy, the most intense wave generation takes place for the He^+-mode in the frequency range $\Omega_{O^+} < \omega < \Omega_{He^+}$ [see, e. g., *Kozyra et al.*, 1984; *Horne and Thorne*, 1993; *Khazanov et al.*, 2003]. (Actually only left-hand polarized waves grow, and the corresponding wave frequencies should be in the range between the cross-over frequency and Ω_{He^+} if the wave normal angle is $\theta \neq 0$.) In the present study we consider only this EMIC wave mode (the other wave modes will be discussed in the further publications). The typical ray trajectories for this wave mode are illustrated in Figures A3–A5. Note that we do not present the evolution of wave numbers, k, in Figures A1–A7, because they can be easily found from the local dispersion equation, $G = 0$, by using the function (5). Ray tracing simulations for the He^+-mode of EMIC waves demonstrate that (1) these waves are well guided along the magnetic field line, and they experience "fast" quasi-periodical bouncing between the surfaces which are very close to the surfaces of $O^+ - He^+$ bi-ion hybrid frequency in the opposite hemispheres, (2) the wave normal angle is oscillating about $\theta = \pi/2$ and progressively, but "slowly," goes to 90 degrees, and (3) the ray L shell coordinate is also "slowly" drifting. *Horne and Thorne* [1993] have demonstrated that the He^+-mode experiences significant energy gain mainly in the vicinity of the plasmapause where the magnetic field gradient which increases wave normal angle can be compensated by the steep plasma density gradient. The ray phase path for the He^+-mode in the vicinity of the plasmapause is illustrated in Figure A5, and the typical timescales for "fast" and "slow" motions which we introduced above may be estimated as $\tau_{fast} \sim 10^2$ s, and $\tau_{slow} \sim 10^3$ s. Another timescale which characterizes the wave evolution is a typical growth time, and this time may be evaluated as $\tau_{growth} = 1/\gamma \sim 10^3$ s. The stated time hierarchy gives us a clue that the bounce-averaged approximation which we have employed in the previous papers [*Khazanov et al.*, 2002, 2003], is still an appropriate approach in order to integrate the wave kinetic equation (6). It should be noted, at the same time, that the bounce-averaging procedure is essentially different in the present study due to the explicitly included EMIC wave propagation and refraction.

[14] The general solution for equation (6) may be obtained by integrating this equation along its characteristics and can be written in the form of

$$\begin{aligned} W(\mathbf{r},t,\mathbf{k}) = W\Bigg(&\mathbf{r} - \int_0^t \dot{\mathbf{r}}(\mathbf{r}(t'),\mathbf{k}(t'))\mathrm{d}t', t = 0, \\ &\mathbf{k} - \int_0^t \dot{\mathbf{k}}(\mathbf{r}(t'),\mathbf{k}(t'))\mathrm{d}t'\Bigg) \\ &\times \exp\left(2\int_0^t \Gamma(\mathbf{R_0},\tau,\mathbf{K_0})\mathrm{d}\tau\right), \end{aligned} \quad (7)$$

$$\begin{aligned} \Gamma(\mathbf{R_0},\tau,\mathbf{K_0}) = \gamma\Bigg(&\mathbf{R_0} + \int_0^\tau \dot{\mathbf{r}}(\mathbf{r}(t'),\mathbf{k}(t'))\mathrm{d}t', \tau, \\ &\mathbf{K_0} + \int_0^\tau \dot{\mathbf{k}}(\mathbf{r}(t'),\mathbf{k}(t'))\mathrm{d}t'\Bigg), \end{aligned} \quad (8)$$

$$\begin{aligned} \mathbf{R_0} &= \mathbf{r} - \int_0^t \dot{\mathbf{r}}(\mathbf{r}(t'),\mathbf{k}(t'))\mathrm{d}t', \\ \mathbf{K_0} &= \mathbf{k} - \int_0^t \dot{\mathbf{k}}(\mathbf{r}(t'),\mathbf{k}(t'))\mathrm{d}t', \end{aligned} \quad (9)$$

where $\mathbf{r}(t) \equiv \mathbf{r}(\mathbf{R_0}, t, \mathbf{K_0})$, and $\mathbf{k}(t) \equiv \mathbf{k}(\mathbf{R_0}, t, \mathbf{K_0})$ are solutions of the ray tracing equations (1)–(4), $\dot{\mathbf{r}} = d\mathbf{r}/dt = \mathbf{v_g} = \partial\omega/\partial\mathbf{k}$, $\dot{\mathbf{k}} = d\mathbf{k}/dt = -\partial\omega/\partial\mathbf{r}$, $\mathbf{R_0}$ and $\mathbf{K_0}$ are the initial

radius vector and wave normal vector, respectively. Argument $t = 0$ in the right-hand side of equation (7) just emphasizes the fact that W is an initial power spectral density distribution for the EMIC waves. For the purpose of the present study, we do not need to resolve equation (6) on the timescale less then τ_{fast}. Then for any particular $\mathbf{r}$ and $\mathbf{k}$, this fact allows us to average both sides of equation (7) over the "fast" wave bounce period, T_g,

$$\langle W(\mathbf{r},t,\mathbf{k})\rangle = \frac{1}{T_g}\int_t^{t+T_g} W(\mathbf{R_0}+\mathbf{r}(t'),t,\mathbf{K_0} + \mathbf{k}(t'))\mathrm{d}t' = \langle W(\mathbf{R_0},t,\mathbf{K_0})\rangle, \tag{10}$$

$$T_g \equiv T_g(\mathbf{R_0},\mathbf{K_0}) = \oint \frac{\mathrm{d}\lambda}{d\lambda/dt}. \tag{11}$$

The averaging in equation (10) is performed along the ray phase trajectory. It is obvious that $\langle W\ (\mathbf{r},\ t,\ \mathbf{k})\rangle$ does not depend on a coordinate along the ray phase path, and now we are able to track power spectral density in the equatorial plane only. In the equatorial plane the wave raypath has coordinates $\mathbf{r_0}$, $\mathbf{k_0}$, and their "slow" time change is described by the following equations:

$$\frac{d\mathbf{r_0}}{dt} = \dot{\mathbf{r}}_0 = \frac{1}{T_g(\mathbf{r_0},\mathbf{k_0})}\int_0^{T_g}\dot{\mathbf{r}}(t)\mathrm{d}t = \frac{1}{T_g(\mathbf{r_0},\mathbf{k_0})}\oint \dot{\mathbf{r}}(\lambda)\frac{\mathrm{d}\lambda}{d\lambda/dt}, \tag{12}$$

$$\frac{d\mathbf{k_0}}{dt} = \dot{\mathbf{k}}_0 = \frac{1}{T_g(\mathbf{r_0},\mathbf{k_0})}\int_0^{T_g}\dot{\mathbf{k}}(t)\mathrm{d}t = \frac{1}{T_g(\mathbf{r_0},\mathbf{k_0})}\oint \dot{\mathbf{k}}(\lambda)\frac{\mathrm{d}\lambda}{d\lambda/dt}, \tag{13}$$

In order to write down equations (12), (13) explicitly, we have to (1) find solutions for the system of ray tracing equations (1)–(4), (2) substitute these solutions into the right-hand side of the equations (1)–(4), and (3) average the result over a "fast" time period, T_g. Note that equations (1)–(4) are written in the coordinate systems specified in section 2, and only for the sake of brevity we write equations (12), (13) in a vector form. Further, keeping in mind that $t \gg T_g$, after straightforward manipulations the system (7), (8) takes the form of

$$\langle W(\mathbf{r_0},t,\mathbf{k_0})\rangle = \left\langle W\left(\mathbf{r_0} - \int_0^t \dot{\mathbf{r}}_0(t')\mathrm{d}t', t=0,\ \mathbf{k_0} - \int_0^t \dot{\mathbf{k}}_0(t')\mathrm{d}t'\right)\right\rangle \times \exp\left(2\int_0^t \langle\Gamma(\overline{\mathbf{R}}_\mathbf{0},\tau,\overline{\mathbf{K}}_\mathbf{0})\rangle\mathrm{d}\tau\right), \tag{14}$$

$$\langle\Gamma(\overline{\mathbf{R}}_\mathbf{0},\tau,\overline{\mathbf{K}}_\mathbf{0})\rangle = \left\langle\gamma\left(\overline{\mathbf{R}}_\mathbf{0} + \int_0^{\tau-T_g}\dot{\mathbf{r}}_0(t')\mathrm{d}t', \tau,\ \overline{\mathbf{K}}_\mathbf{0} + \int_0^{\tau-T_g}\dot{\mathbf{k}}_0(t')\mathrm{d}t'\right)\right\rangle \approx \left\langle\gamma\left(\overline{\mathbf{R}}_\mathbf{0} + \int_0^{\tau}\dot{\mathbf{r}}_0(t')\mathrm{d}t', \tau,\ \overline{\mathbf{K}}_\mathbf{0} + \int_0^{\tau}\dot{\mathbf{k}}_0(t')\mathrm{d}t'\right)\right\rangle, \tag{15}$$

$$\langle\gamma(\overline{\mathbf{R}}_\mathbf{0},\tau,\overline{\mathbf{K}}_\mathbf{0})\rangle = \frac{1}{T_g(\overline{\mathbf{R}}_\mathbf{0},\overline{\mathbf{K}}_\mathbf{0})}\int_0^{T_g}\gamma\left(\overline{\mathbf{R}}_\mathbf{0} + \int_0^t\dot{\mathbf{r}}(t')\mathrm{d}t', \tau,\ \overline{\mathbf{K}}_\mathbf{0} + \int_0^t\dot{\mathbf{k}}(t')\mathrm{d}t'\right)\mathrm{d}t, \tag{16}$$

$$\overline{\mathbf{R}}_\mathbf{0} = \mathbf{r_0} - \int_0^t\dot{\mathbf{r}}_0(t')\mathrm{d}t', \qquad \overline{\mathbf{K}}_\mathbf{0} = \mathbf{k_0} - \int_0^t\dot{\mathbf{k}}_0(t')\mathrm{d}t', \tag{17}$$

where $\overline{\mathbf{R}}_\mathbf{0}$, and $\overline{\mathbf{K}}_\mathbf{0}$ are equatorial initial values for the radius vector and wave normal vector, respectively.

[15] Solution (14)–(17) completely describes the evolution of the bounce-averaged EMIC wave power spectral density if all the plasma properties and initial distribution, W, are specified. An averaged wave power spectral density, $\langle W\rangle$, should satisfy a transport equation similar to the differential equation (6), and this transport equation has the following form:

$$\frac{\partial\langle W(\mathbf{r_0},t,\mathbf{k_0})\rangle}{\partial t} + \dot{\mathbf{r}}_0\cdot\frac{\partial\langle W\rangle}{\partial\mathbf{r_0}} + \dot{\mathbf{k}}_0\cdot\frac{\partial\langle W\rangle}{\partial\mathbf{k_0}} = 2\langle\gamma(\mathbf{r_0},t,\mathbf{k_0})\rangle\cdot\langle W\rangle, \tag{18}$$

where $\dot{\mathbf{r}}_\mathbf{0} = \partial\omega\ (\mathbf{r_0},\ \mathbf{k_0})/\partial\mathbf{k_0}$, $\dot{\mathbf{k}}_\mathbf{0} = -\partial\omega(\mathbf{r_0},\ \mathbf{k_0})/\partial\mathbf{r_0}$, and the timescale for equation (18) is in the range $\tau_{fast} \ll \Delta t \ll \tau_{slow}$. Substituting the solution (14)–(17) in the equation (18), it is easy to verify that indeed the left-hand side in the equation is equal to the right-hand side. Note that equation (18) can also be obtained by applying a corresponding bounce averaging procedure to the original wave kinetic equation (6).

[16] It is more convenient to characterize the EMIC wave power spectral density by frequency and equatorial wave normal angle instead of the wave vector, $\mathbf{k_0}$, [see, e.g., *Lyons and Williams*, 1984; *Khazanov et al.*, 2002, 2003]. The transformation into (ω, θ_0) is straightforward, and we write down only the resulting form of equation (18) in these new variables,

$$\frac{\partial\langle W\rangle}{\partial t} + \dot{r}_0\cdot\frac{\partial\langle W\rangle}{\partial r_0} + \dot{\theta}_0\cdot\frac{\partial\langle W\rangle}{\partial\theta_0} = 2\langle\gamma(r_0,\varphi,t,\omega,\theta_0)\rangle \times\langle W(r_0,\varphi,t,\omega,\theta_0)\rangle, \tag{19}$$

where

$$\dot{\theta}_0 = \frac{d\theta_0}{dt} = \frac{1}{T_g(r_0,\varphi,\omega,\theta_0)}\oint\left(k_\lambda\frac{dk_r}{dt} - k_r\frac{dk_\lambda}{dt}\right)\frac{\mathrm{d}\lambda}{k^2 d\lambda/dt}. \tag{20}$$

In equations (19), (20) we took into account the fact that vector $\mathbf{r_0}$ has only one component for 2D ray propagation, and also emphasized the parametric dependency for the functions on geomagnetic longitude, φ.

3.2. Tunneling of EMIC Waves Across Reflection Region

[17] The employed wave kinetic equation (6) treats waves as quasi-particles, and according to ray tracing simulations based on the system (1) –(4), these quasi-particles bounce

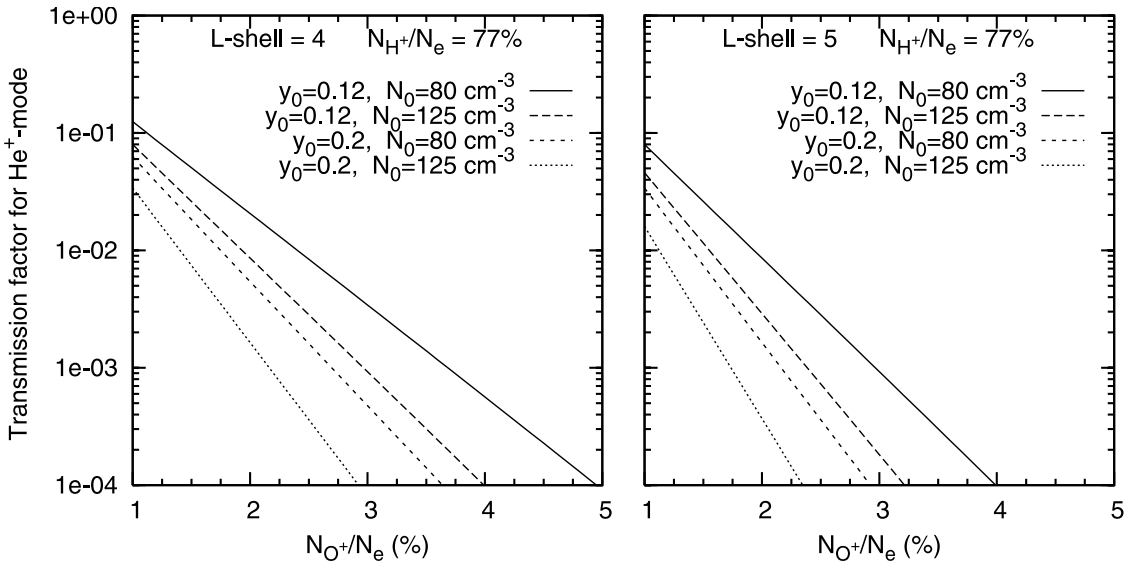

Figure 2. Transmission factors for He^+-mode of EMIC waves versus relative abundance of plasmaspheric O^+ ions are shown. Results from combinations of two equatorial densities and normalized wave frequencies are presented for L = 4, and L = 5. Note that we use the same equatorial electron densities for both L = 4 and L = 5 in order to demonstrate "pure" L shell dependence. In all the cases we keep $\eta_1 = 0.77$, and equation $\eta_1 + \eta_2 + \eta_3 = 1$ is held.

between surfaces of the bi-ion hybrid frequency in opposite hemispheres. It is clear that a "geometric optics" approximation is not valid near the reflection points, and a full wave description is required to analyze wave propagation in these regions [see, e.g., *Stix*, 1992]. In order to explain simultaneous measurements of EMIC waves by the GEOS spacecrafts and in the vicinity of their magnetic footprints, *Perraut et al.* [1984] have demonstrated that for EMIC waves of class *III*, generated at the geomagnetic equator, some part of wave energy can tunnel through the region of reflection in $H^+ - He^+$ thermal plasma, and these waves can be detected on the ground. We generalize and quantify the effect of wave tunnelling for the case under consideration in the present study, namely, for the He^+-mode of EMIC waves propagating in a multispecies ($e - H^+ - He^+ - O^+$) magnetosphere. The detailed derivation of the wave transmission (tunnelling) factor is presented in Appendix B.

[18] The transmission factor T, depends on L shell, equatorial electron density and normalized wave frequency, but most dramatically T depends on a fraction of O^+ ions that determines the width of the stop zone. All these dependences are illustrated in Figure 2. Note that we use the same equatorial electron densities for both L = 4 and L = 5 in order to demonstrate "pure" L shell dependence. We can see from Figure 2 that the smaller EMIC wave frequency the larger transmission factor. This result is in agreement with the conclusion of *Perraut et al.* [1984] that "the transmission through the stop zone induced by the presence of He^+ ions in the magnetospheric plasma is a low-frequency bypass filter." Dependence of the transmission factor on plasma density just reflects the fact that the larger the plasma density the smaller the EMIC wavelength and as a consequence the less wave energy that can be transmitted through the stop zone. The effect of an increase in the transmission coefficient by decreasing the L shell can reveal itself during the main and early recovery phases of a geomagnetic storm, when the wave generation regions move closer to Earth. The plasmaspheric thermal O^+ ion abundance is about 1–5% in quiet geomagnetic conditions [*Horwitz et al.*, 1981], and we present all the results in Figure 2 for this range. It is obvious that the amount of O^+ ions controls the width of another stop zone, to which the transmission coefficient will be very sensitive. The growth rate for the He^+-mode has maximum at a y_0 of about 0.12 [*Khazanov et al.*, 2003], and as follows from Figure 2, the transmission factor $T \approx 10\%$ for L = 4, $y_0 = 0.12$, and $\eta_3 = 1\%$. In the current study we assume that thermal plasmaspheric plasma consists of H^+, He^+, and O^+ ions with ratios to electron content 0.77, 0.20, and 0.03, respectively. For $y_0 = 0.12$, L = 4, and $\eta_3 = 0.03$, the transmission factor is $T \approx 0.003$ as follows from Figure 2. So only a minor portion of the EMIC wave energy (about T^2) can tunnel across the reflection region. This fact allows us to ignore the effect of tunnelling in the wave kinetic equation for the He^+-mode and safely use the earlier derived equation (19).

[19] In conclusion of this subsection we note the following. (1) In addition to the tunnelling of the He^+-mode, the equations obtained in Appendix B also allow us to analyze the tunnelling of the H^+-mode of EMIC waves through the $He^+ - H^+$ stop zone (note that the O^+-mode of EMIC waves reflects from the ionosphere altitudes). (2) The component of the wave vector parallel to the external magnetic field comes to zero at the reflection surface, and EMIC wave energy is not absorbed through resonant processes [see, e.g., *Rauch and Roux*, 1982; *Stix*, 1992]. So only reflection and transmission are possible in the vicinity of the surface.

4. RC-EMIC Wave Model

4.1. Governing Equations

[20] We simulate RC dynamics by solving the bounce-averaged kinetic equation for the phase space distribution

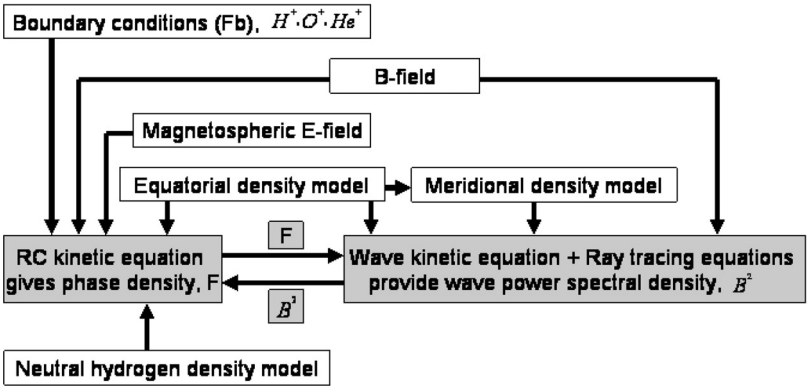

Figure 3. A block diagram of our self-consistent model of magnetospheric RC ions and propagating EMIC waves is shown.

functions, $F(r_0, \varphi, E, \mu_0, t)$, for each RC species ($H^+$, O^+, and He^+). The distribution function depends on the radial distance in the magnetic equatorial plane r_0 (zero at the Earth's center), geomagnetic east longitude (zero at midnight), kinetic energy E, cosine of the equatorial pitch angle μ_0, and time t. The model based on this equation was originally developed at the University of Michigan [*Fok et al.*, 1993; *Jordanova et al.*, 1996a], and it has been called the ring current-atmosphere interaction model (RAM). There are now several branches of this model currently in use, namely those at NASA Goddard Space Flight Center [*Fok et al.*, 2003; *Ebihara et al.*, 2004, 2005], the University of New Hampshire [*Jordanova et al.*, 2003], the University of Michigan [*Kozyra et al.*, 2002; *Liemohn et al.*, 2004], and NASA Marshall Space Flight Center [*Khazanov et al.*, 2003].

[21] In order to describe the bounce-averaged evolution of the wave power spectral density for the He^+-mode, we use the governing equation (19) along with equation (20), and the system of the ray tracing equations (1)–(4). We should note that (1) the third term in the left-hand side of equation (19), as a rule, is greater than the second one, and in this study we ignore the slow radial drift for waves, and (2) power spectral density W, for EMIC waves is mostly represented by magnetic wave energy. Thus the resulting system of two governing equations can be written as

$$\frac{\partial F}{\partial t}+\frac{1}{r_0^2}\frac{\partial}{\partial r_0}\left(r_0^2\left\langle\frac{dr_0}{dt}\right\rangle F\right)+\frac{\partial}{\partial\varphi}\left(\left\langle\frac{d\varphi}{dt}\right\rangle F\right)+\frac{1}{\sqrt{E}}\frac{\partial}{\partial E}\left(\sqrt{E}\left\langle\frac{dE}{dt}\right\rangle F\right)+\frac{1}{\mu_0 h(\mu_0)}\frac{\partial}{\partial\mu_0}\left(\mu_0 h(\mu_0)\left\langle\frac{d\mu_0}{dt}\right\rangle F\right)=\left\langle\left(\frac{\delta F}{\delta t}\right)_{loss}\right\rangle, \quad (21)$$

$$\frac{\partial B^2}{\partial t}+\langle\dot{\theta}_0\rangle\cdot\frac{\partial B^2}{\partial\theta_0}=2\langle\gamma(r_0,\varphi,t,\omega,\theta_0)\rangle\times B^2(r_0,\varphi,t,\omega,\theta_0), \quad (22)$$

In the left-hand side of the equation (21) all the bounce-averaged drift velocities are denoted as $\langle\cdots\rangle$, and may be found in previous studies [*Jordanova et al.*, 1994; *Khazanov et al.*, 2003]. Note that in order to keep uniformity between equations (21) and (22), there are redesignations $\langle B^2\rangle \rightarrow B^2$ and $\dot{\theta}_0 \rightarrow \langle\dot{\theta}_0\rangle$ are made in equation (22) compared with equation (19). The term in the right-hand side of (21) includes losses from charge exchange, Coulomb collisions, ion-wave scattering, and precipitation at low altitudes [*Jordanova et al.*, 1996a, 1997; *Khazanov et al.*, 2003]. Loss through the dayside magnetopause is taken into account allowing a free outflow of the RC ions from the simulation domain. The bounce-averaged pitch angle diffusion coefficient in the right-hand side of (21) is a functional (not a function!) of the EMIC wave power spectral density, B^2, i.e., $\langle D_{\mu_0,\mu_0}\rangle = \langle D_{\mu_0}, \mu_0\ (B^2(\cdot))\rangle$, which is governed by the wave kinetic equation (22). On the other hand, $\langle\gamma(r_0, \varphi, t, \omega, \theta_0)\rangle$ in equation (22) is a functional of the phase space distribution function, F, i.e., $\langle\gamma\rangle = \langle\gamma\ (F(\cdot))\rangle$ [*Khazanov et al.*, 2003]. So the system (21), (22) self-consistently describes the interacting RC and EMIC waves in a quasi-linear approximation. A block diagram of the self-consistent RC-EMIC wave model is presented in Figure 3. It should be emphasized that in order to describe wave-particle interaction in equation (21) we have to know the off-equatorial power spectral density distribution for EMIC waves, and this distribution can be easily mapped from the magnetic equator by using solutions of the ray tracing equations (1)–(4).

[22] Simulation of the RC dynamics itself is based on the bounce-averaged kinetic equation, and this equation is the same as that used in our previous studies. This equation and the involved numerical algorithms are described by *Jordanova et al.* [1996a, 1997] and *Khazanov et al.* [2003] in detail. However, in comparison with our previous RC-EMIC wave model [*Khazanov et al.*, 2002, 2003], the modeling of the wave's dynamics is importantly different in the present study. In order to describe the EMIC wave's evolution we explicitly include the ray tracing equations in our previous self-consistent model, and use the general form of the wave kinetic equation. This is a crucial new feature of the present model and, to the best of our knowledge, ray tracing equations are for the first time explicitly employed on a global magnetospheric scale in order to simulate spatial, temporal, and spectral evolutions of the RC-EMIC wave system. The differences between equation (22) and the wave kinetic equation that was used in our previous studies can be summarized as follows. In the present study (1) the case of multispecies ($e - H^+ - He^+ - O^+$) plasma is considered, (2) wave propagation and refraction are rigorously taken into account in the full wave

kinetic equation, (3) there is no wave reflection from the ionosphere (compare with *Khazanov et al.* [2002, 2003, equation (2)]) because the He^+-mode reflects from the surfaces of the $O^+ - He^+$ bi-ion hybrid frequency in a multi-ion plasma, and currently we do not include the tunnelling of the waves across the corresponding stop zone. It should be noted, at the same time, that nonperfect wave reflection can easily be incorporated in equation (22) by calculating the corresponding reflection coefficients by using the equations of Appendix B.

4.2. Approaches and Initial/Boundary Conditions Used in Simulation

[23] The geomagnetic field, B, used in our simulation, is taken to be a dipole field. The electric field is expressed as the shielded (factor of 2) Volland-Stern-type convection field [*Volland*, 1973; *Stern*, 1975] which is Kp-dependent, and a corotation field [e.g., *Lyons and Williams*, 1984]. The equatorial cold electron density distribution, n_{e0}, is calculated with the time-dependent equatorial model of *Rasmussen et al.* [1993]. For modeling the RC-EMIC wave interaction and wave propagation we need the density distribution in the meridional plane also. In the present study we employ an analytical density model which includes the product of three terms (1) diffusive equilibrium model term [*Angerami and Thomas*, 1964], (2) lower ionosphere factor, and (3) plasmapause and outer magnetosphere term. This analytical model is adjusted to the *Rasmussen* model at the equator, so the resulting plasmaspheric density model provides 3-D spatial distributions for electrons and H^+, He^+, O^+ ion species. Geocoronal neutral hydrogen number densities, needed to calculate loss due to charge exchange, are obtained from the spherically symmetric model of *Chamberlain* [1963] with its parameters given by *Rairden et al.* [1986]. Plasmaspheric core plasma is assumed to consist of electrons, 77% of H^+, 20% of He^+, and 3% of O^+, which are in the range of 10–30% for He^+ and 1–5% for O^+ following observations by *Young et al.* [1977] and *Horwitz et al.* [1981]. An initial study of the RC development during the May 1998 storm period was presented by *Farrugia et al.* [2003], who used the RC kinetic model of *Jordanova et al.* [1998a] to model Dst variation during the storm and to calculate the energy content for the major RC ion species, H^+, O^+, and He^+. They found that during this storm the energy density of H^+ is greater than twice that of O^+ at all MLTs, and the contribution of He^+ to the RC energy content is negligible. This result allows us to assume in the present study that the RC is entirely made up of energetic protons, and to ignore the RC O^+ and He^+ ions in the simulation.

[24] The nightside boundary condition is imposed at the geostationary distance, and it is obtained using flux measurements from the Magentospheric Plasma Analyzer (MPA) and the Synchronous Orbit Particle Analyzer (SOPA) instruments on the geosynchronous LANL satellites during the modeled event [*Khazanov et al.*, 2003]. To obtain the self-consistent initial conditions for equations (21) and (22), the simulation was started at 0000 UT on 1 May, 1998 using a background noise level for the He^+-mode of EMIC waves [see, e.g., *Akhiezer et al.*, 1975], the statistically derived quiet time RC proton energy distribution of *Sheldon and Hamilton* [1993], and the initial pitch angle characteristics of *Garcia and Spjeldvik* [1985]. The RC energy distribution is constructed from measurements of the charge-energy-mass (CHEM) spectrometer on board the AMPTE/CCE satellite during the quiet conditions with $|Dst| < 11$ nT and $Kp < 2^+$. The pitch angle characteristics are derived from the quiet time radiation belt ion data of instruments flown on Explorer 45. In about 20 hours of evolution the wave magnetic energy distribution reaches a quasi-stationary state indicating that the RC-EMIC wave system achieves a quasi-self-consistent state. So, the self-consistent modeling of the May 1998 storm period is started at 0000 UT on 2 May (24 hours after 1 May 0000 UT) using solutions of the equations (21) and (22) at 2400 UT on 1 May as the initial conditions for further simulation. At this time a narrow region of EMIC wave activity is observed in the nighttime MLT sector with typical wave magnetic field amplitudes of order 1 nT or less.

5. Global Evolution and Spectral Distributions of He^+-Mode of Propagating EMIC Waves

[25] Using our newly developed model we simulate the May 1998 storm. Although this storm has been studied before [see, e.g., *Khazanov et al.*, 2002, 2003], we make this simulation for benchmark purposes. Let us first recall the geomagnetic conditions during this event. The three geomagnetic indices for the 2–7 May 1998 period are shown in Figure 4, and reflect the changing geomagnetic conditions. The interplanetary configuration of 1–7 May 1998 consists of a coronal mass ejection (CME) interacting with a trailing faster stream [*Farrugia et al.*, 2003]. The CME drives an interplanetary shock observed by instruments aboard the WIND spacecraft at about 2220 UT on May 1. Four episodes of the large negative north-south IMF component, B_Z, are monitored. The first episode starts at ~0400 UT on 2 May (28 hours after 1 May 0000 UT), the second at 0230 UT on 4 May (74.5 hours after 1 May 0000 UT), and the third and fourth at ~0200 UT and ~1200 UT on 5 May (98 and 108 hours after 1 May 0000 UT, respectively). These caused a "triple-dip" storm with minimums $Dst = -106$ ($Dst^* = -75$) nT, $Dst = -272$ ($Dst^* = -195$) nT, and $Dst = -153$ ($Dst^* = -103$) nT. (The fourth episode of $B_Z < 0$ is not so strongly pronounced in *Dst*, but all the episodes are well correlated with the peaks of *Kp*.) The planetary Kp index reached maximum values $Kp \approx 7^-$ and $Kp \approx 9^-$ at the times when Dst minimums were recorded (see Figure 4, top and bottom). The AE index during 2–7 May 1998 is shown in the middle panel of Figure 4. Several peaks, corresponding to *Kp* peaks, are seen with a maximum $AE \approx 2340$ nT at the time when the absolute maximum of Kp index is observed.

[26] In order to demonstrate the effects of EMIC wave propagation and refraction on the wave energy distributions and evolution, we select two time intervals during the storm. The first interval takes place on 2 May, from 2400 UT to 4800 UT after 1 May, 0000 UT, and covers the period of the first *Dst* dip. The second one from 7200 UT to 8600 UT after 1 May, 0000 UT represents the period of largest *Dst* decrease on 4 May. We shall present below some of our new results and compare them with results based on a different EMIC wave treatment that was adopted in an earlier, RAM-based, global model [*Kozyra et al.*, 1997].

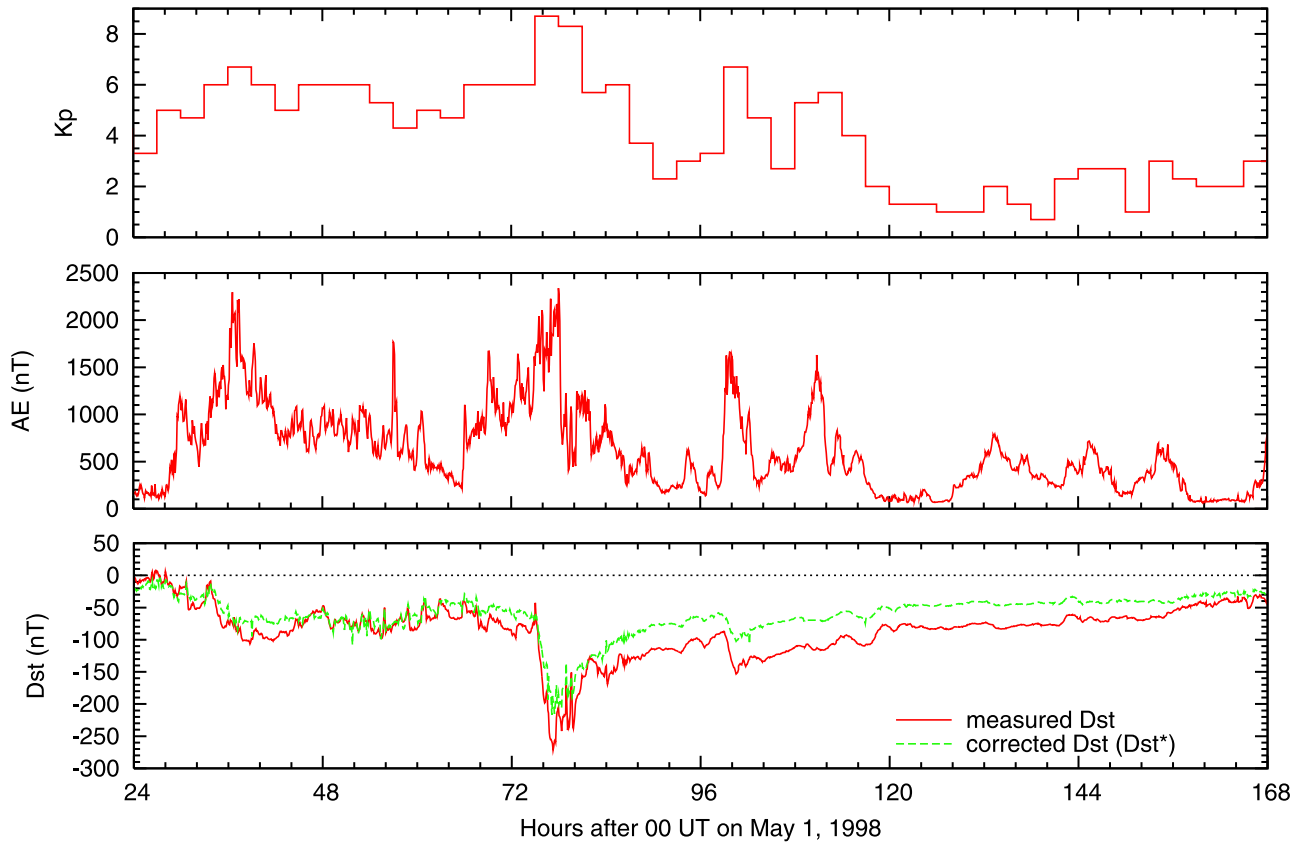

Figure 4. Geomagnetic indices for the 2–7 May 1998 storm period are shown. (top) Three-hour *Kp* index; (middle) *AE* index which is calculated from the data of 67 stations with magnetic latitudes between 55 and 76 degrees; (bottom) *Dst* indices. *Dst* index is calculated after measurements from 26 stations with magnetic latitudes below 40°. *Dst** is a *Dst* index corrected for the Chapman-Ferraro current, the quiet time current, and the effect of the Earth's induction as $Dst^* = (Dst - c_1 P_{dyn}^{1/2} + c_2)/\xi$, where c_1 = 15.8 nT/nPa$^{1/2}$, c_2 = 20 nT, coefficient for the induction is ξ = 1.5 [e. g., *Ebihara and Ejiri*, 2000], and the 30 min time lag between WIND and Earth is adopted after *Farrugia et al.* [2003].

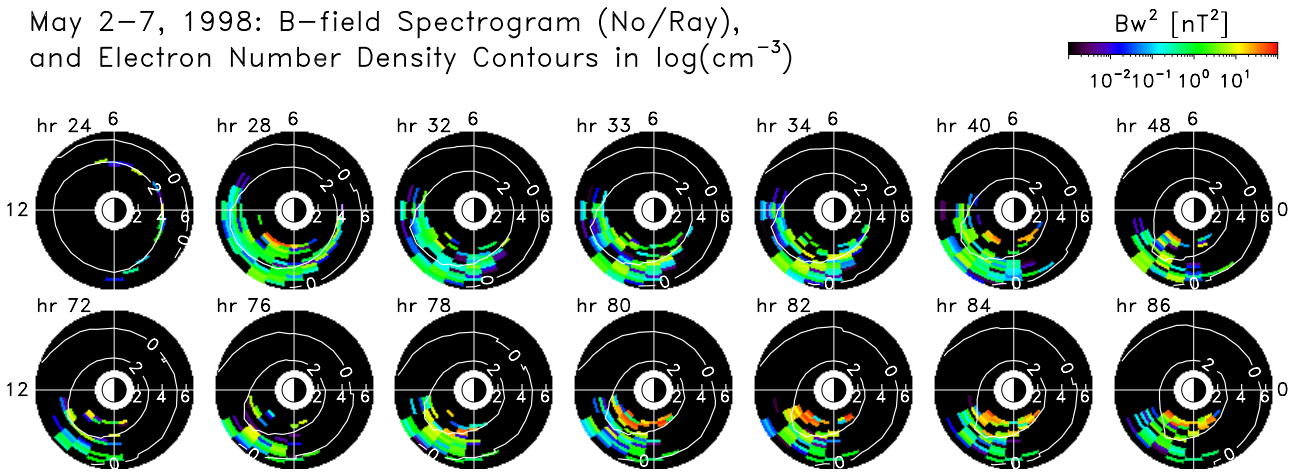

Figure 5. Snapshots of the equatorial (MLT, L shell) distributions of squared wave magnetic field for the He^+-mode are shown. The results are obtained by employing our previous model [*Khazanov et al.*, 2003] in which wave propagation along geomagnetic field lines has been assumed, and wave refraction has been ignored. The thermal plasmaspheric plasma consists of electrons, 77% of H^+, 20% of He^+, and 3% of O^+. The white lines are the contours of equatorial plasmaspheric electron density, and all specified hours are counted from 0000 UT on 1 May 1998.

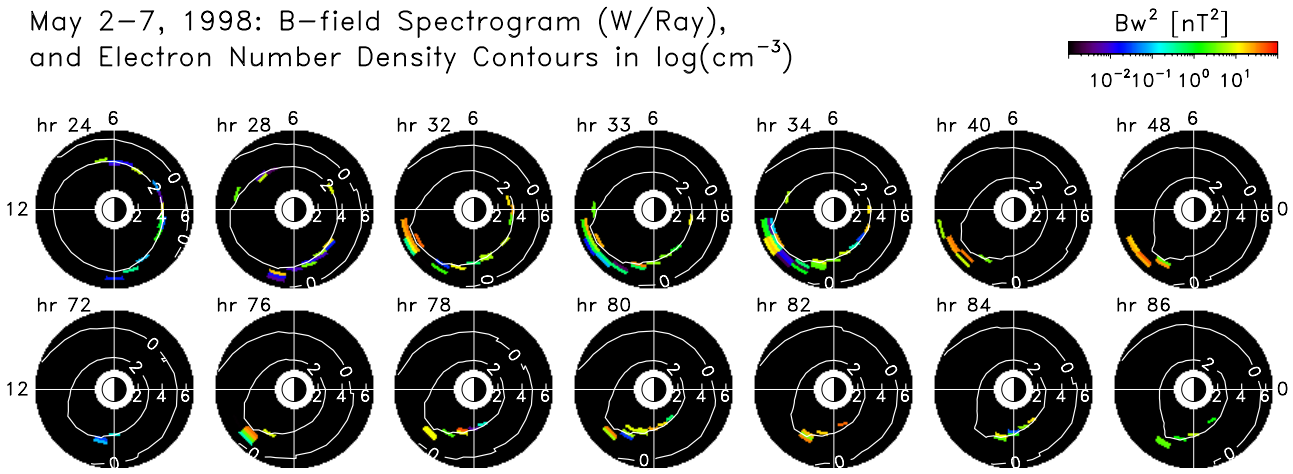

Figure 6. Same as Figure 5, except *B* field distributions are obtained by solving equations (21) and (22), i.e., wave propagation and refraction are calculated by solving equations (1)–(4), and ray propagating effects are explicitly taken into account in the wave kinetic equation.

5.1. Global Distribution and Evolution of He^+-Mode

[27] In comparison with our earlier published results [*Khazanov et al.*, 2003], in the present study we consider the case of the He^+-mode in multi-ion thermal plasma. So it should be very helpful first to present the results from our previous model, except for the case of a multi-ion plasmasphere. The equatorial (MLT, L shell) distributions of the squared wave magnetic field,

$$B_w^2(r_0,\varphi,t) = \int_{\omega_{\min}}^{\omega_{\max}} d\omega \int_0^{\pi} d\theta_0 B^2(r_0,\varphi,t,\omega,\theta_0),$$

are shown in Figure 5 for the He^+-mode of the EMIC waves. These results are obtained by using our old model [*Khazanov et al.*, 2003] in which the wave propagation along geomagnetic field lines has been assumed and wave refraction has been ignored. The thermal plasma consists of electrons, 77% of H^+, 20% of He^+, and 3% of O^+. White lines in the Figure show the contours of equatorial plasmaspheric electron density, and all the specified hours are counted from 0000 UT on 1 May. As stated above, in order to obtain the self-consistent initial conditions for equations (21) and (22), we ran the model for 24 hours on 1 May, including the ray tracing equations in the model. Then, at 0000 UT on 2 May, we turn off the ray tracing, and replaced equation (22) with equation (2) from *Khazanov et al.* [2003]. It follows from Figure 5 that at 24 hours after 1 May, 0000 UT, the wave activity is mainly concentrated in the night MLT sector, and the wave active zones are very well organized by the plasmapause location. Later, on 2 and 4 May, we observe wave activity predominantly in the postnoon-premidnight MLT sector with a very wide radial extension. *Horne and Thorne* [1993] have demonstrated that "even though the local spatial growth rates increase as we move from inside to outside the plasmapause, propagation effects show that the largest amplification can occur near the plasmapause density gradient for L < 7." So the results in Figure 5 can only be treated as rough distributions of wave power, and we provide them only for reference and comparison purposes.

[28] The new results obtained from simulation based on the developed system of governing equations (21) and (22) are presented in Figure 6. There is a very impressive qualitative difference between the EMIC wave energy distributions in Figure 6 and in Figure 5. In comparison to the results in Figure 5, the *B* field distributions in Figure 6 are highly organized by location of the plasmapause gradient, and a maximum of $B^2 \simeq 50$ nT^2 is observed in the dusk MLT sector shortly after absolute *Dst* minimum; MLT = 17, L = 3.5, at 78 hours after 1 May, 0000 UT. Analyzing the results of ray tracing simulations, *Horne and Thorne* [1993] have shown that at the plasmapause the density gradient counteracts refraction caused by the magnetic field gradient and curvature. As a result, net refraction is suppressed, and the He^+-mode grows preferably at the plasmapause. Comparing the wave magnetic field distributions in Figure 6 with the density distributions in Figure 7, we can clearly observe this effect in the obtained wave (MLT, L shell) distributions.

[29] In conclusion of this subsection, let us compare the presented global wave distributions with the results of another, RAM-based, global model where a different EMIC wave description has been adopted. *Kozyra et al.* [1997] have incorporated in the RAM model the results of simulations of wave propagation and amplification based on the HOTRAY ray tracing code [*Horne*, 1989]. They have found that the plasmapause density gradient has a major impact on the path-integrated wave gain for the He^+-mode. Further, in order to construct a global model of convective wave gain, these authors (1) approximate phase space distribution functions from the RAM model with bi-Maxwellian distributions, and calculate field-aligned convective growth rates according to *Kozyra et al.* [1984], (2) integrate these growth rates along geomagnetic field lines over ±5° latitude range, and (3) multiply the results of integration by a factor of 2 at the plasmapause, and by a factor of 1.5 at 0.25 R_E distance on both sides of the plasmapause in order to obtain agreement with HOTRAY amplification. After that a Gaussian shape for the EMIC wave power spectral density has been assumed in both wave frequency and wave normal angle, then based on a statistical study they have related the

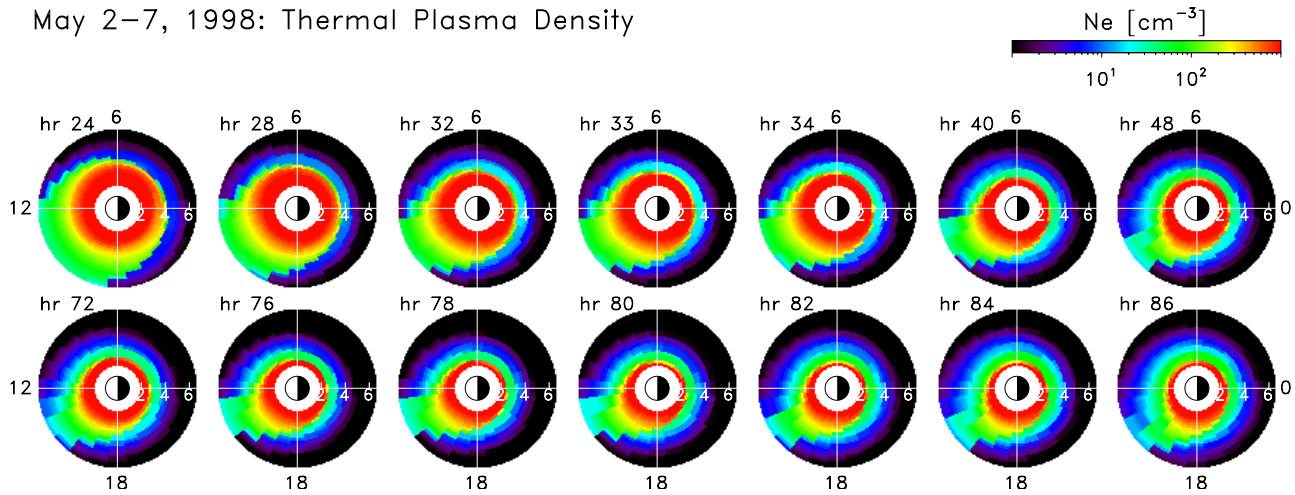

Figure 7. Equatorial plasma density distributions from *Rasmussen et al.* [1993] model are shown. The specified hours are counted from 0000 UT on 1 May 1998.

calculated wave gains to the EMIC wave amplitudes, and have taken into account wave induced RC scattering inside of a ±10° magnetic latitude range. So this branch of the RAM model (for more details see [*Jordanova et al.*, 1997, 2001] and references therein) takes into account some features of the wave propagation and refraction and therefore should be compared with results from our newly developed model.

[30] Using the same RC initial and boundary conditions as we set in our model, we started this version of RAM at 0000 UT on 1 May 1998. The selected equatorial snapshots of the squared wave magnetic field distributions are presented in Figure 8 for the He^+-mode of EMIC waves. We indeed find that EMIC wave activity is preferably localized in the postnoon-premidnight MLT sector, and it is partly controlled by the plasmapause location. Nevertheless in comparison with the results in Figure 6, this wave activity occupies more extended equatorial zones, and we do not observe in Figure 8 that the plasmapause density gradient has a major impact on the wave excitation during the studied storm. Overall, this version of RAM [*Kozyra et al.*, 1997; *Jordanova et al.*, 1997, 2001] produces more extended and less intense equatorial wave distributions during the May 1998 storm period than found by our more complete treatment of RC-EMIC wave interaction.

5.2. Spectral Distributions of He^+-Mode of Propagating EMIC Waves

[31] It is well-known that quasi-linear wave-particle interaction strongly depends on the wave/particle characteristics, particularly on the wave power spectral density which itself is determined by a self-consistent evolution of the wave-particle system. In most studies, to describe a quasi-linear interaction of EMIC waves and RC ions, a Gaussian approximation to the shape of power spectral density is assumed [see, e.g., *Lyons*, 1974; *Jordanova et al.*, 2001]. On the other hand, as follows from the theoretical study by *Khazanov et al.* [2003], the Gaussian distribution is not always a good fit to the form of wave power spectral density. In this paper *Khazanov et al.* [2003] have assumed that the wave distributions are quasi field-aligned, and distributions over wave normal angles are entirely concen-

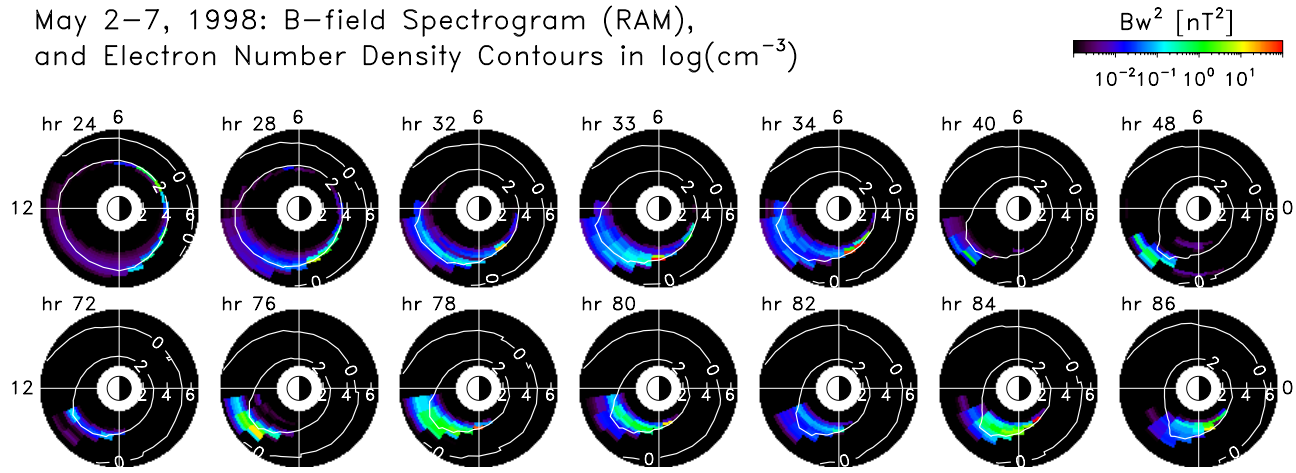

Figure 8. Same as Figure 5, except *B* field distributions are obtained from a simulation employing the RAM model as described by *Kozyra et al.* [1997] and *Jordanova et al.* [2001].

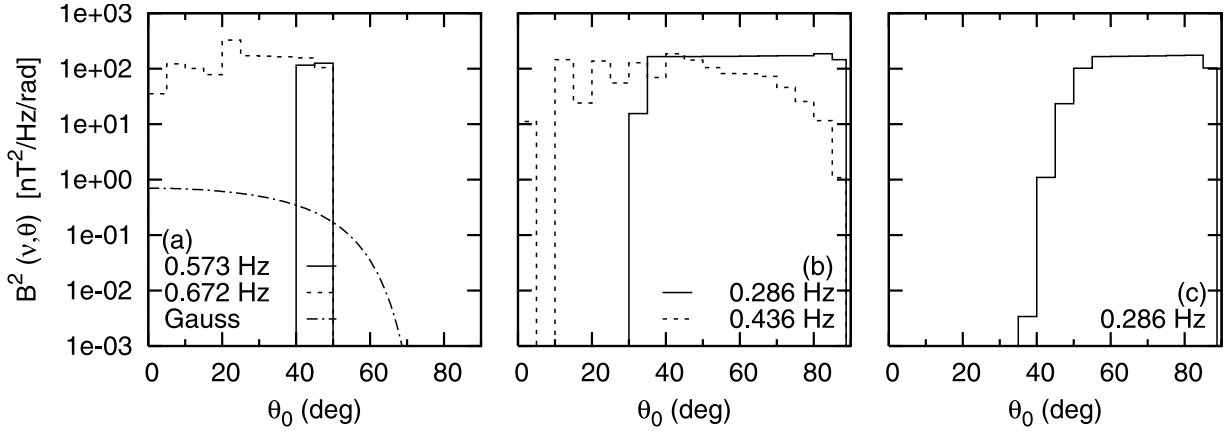

Figure 9. Equatorial spectral distributions for He^+-mode of EMIC waves are shown. All the squared magnetic field spectra are obtained at 48 hours after 0000 UT on 1 May 1998. (a) L = 5.25, MLT = 16, and we present distributions for two wave frequencies, ν = 0.573 Hz (solid line) and ν = 0.672 Hz (dashed line). An unnormalized Gaussian distribution from *Jordanova et al.* [2001] is also presented (dash-dotted line which is valid in the region of $0 < \theta_0 < 45°$ only). (b) L = 5.75, MLT = 15, and there are two distributions for frequencies, ν = 0.286 Hz (solid line) and ν = 0.436 Hz (dashed line). (c) L = 5.75, MLT = 14, and ν = 0.286 Hz.

trated in the regions of $\theta < 27°$ for forward and of $153° < \theta < 180°$ for backward propagation, respectively. So they have integrated the power spectral density over wave normal angle and have only analyzed the shapes of the resulting frequency spectra. We have quite a different situation because wave propagation and refraction are rigorously taken into account. We will next discuss the consequence this causes in the power spectral density distributions over wave normal angle.

[32] As follows from the results of Appendix A, the He^+-mode of EMIC waves bounces between the surfaces of the $O^+ - He^+$ bi-ion hybrid frequency in opposite hemispheres, and the wave normal vector becomes more oblique when the wave packets approach these surfaces ($\theta = 90°$ at the reflection point). So, for the specified wave frequency, there is a quasi-stationary distribution of wave normal angles (and wave normal numbers) between the equatorial plane and reflective surfaces. In comparison with equation (2) from *Khazanov et al.* [2003], the left-hand side in equation (22) is different, and this fact may lead to strong modification of the wave power spectral density distribution. If we put $\dot{\theta}_0 = 0$ in equation (22), then the wave normal angle distribution will be truly stationary (of course, in the case of a stationary medium), and the equatorial EMIC wave power spectral density will be concentrated in the region of "relatively small" equatorial wave normal angles (we mean that the region about 90° will be empty). In reality, $\dot{\theta}_0 \neq 0$, and θ_0 is positive. This leads to energy outflow from the region of small wave normal angles to $\theta_0 = \pi/2$ (see the second term in the left-hand side of equation (22)). The EMIC wave growth rate maximizes for $\theta_0 = 0$ and electron Landau damping has a peak for θ_0 close to 90°. Note that Landau damping disappears at $\theta = 90°$. Then, the resulting power density distribution over wave normal angle depends on the ratios between rates of wave growth (mostly in the region of small θ_0), Landau damping (mostly at large θ_0), and $\dot{\theta}_0/\theta_0$.

[33] In Figure 9 we present energy distributions over equatorial wave normal angle for the He^+-mode of EMIC waves. All the squared magnetic field spectra are shown in the postnoon-dusk MLT sector at 48 hours after 0000 UT on 1 May 1998. We also present in Figure 9a the unnormalized Gaussian distribution from *Kozyra et al.* [1997] and *Jordanova et al.* [2001] which has a maximum at $\theta_0 = 0$, and it is only valid in the region of $0 < \theta_0 < 45°$. Figure 9a demonstrates a typical quasi field-aligned wave normal angle distribution for ν = 0.672 Hz. In this case, wave growth rate in the region of small θ_0 is larger than the outflow rate to the region of greater θ_0. Diametrically opposed cases are presented in Figure 9b for ν = 0.286 Hz and in Figure 9c, where EMIC wave energy is concentrated in the region of large θ_0. The dashed line (ν = 0.436 Hz) in Figure 9b represents an intermediate case. Although power spectral density in the latter case drops dramatically for $\theta_0 > 40°$, there is still a very large B^2 (ν, θ) and we observe spread distribution in the entire wave normal angle region. Almost no presented power spectral density distributions appear as Gaussian functions, and most important that EMIC wave energy can occupy not only the region of generation, i.e., the region of small θ_0, but the entire wave normal angle region and even only the region near $\theta_0 = \pi/2$. The latter, for example, is extremely crucial for energy transfer to thermal plasmaspheric electrons by resonant Landau damping, and subsequent downward heat transport and excitation of stable auroral red arcs [*Cornwall et al.*, 1971]. We shall consider this effect in paper 2 in detail.

6. Conclusions

[34] In this paper we have further developed a self-consistent model of interacting RC ions and EMIC waves [*Khazanov et al.*, 2002; 2003]. The simulation of RC dynamics is based on the bounce-averaged kinetic equation, and this equation is the same as in our previous studies. However, in comparison with our previous RC-EMIC wave model, the modeling of the wave's dynamics is quite different in the present study. In order to describe the EMIC wave's evolution we have explicitly included the ray tracing

equations in our previous self-consistent model and have used the complete wave kinetic equation. This is a crucial new feature of the present model and, to the best of our knowledge, ray tracing equations are for the first time explicitly employed together with a RC model on a global magnetospheric scale to describe the spatial and temporal evolution of the RC-EMIC wave system. The differences between the newly derived kinetic wave equation (22) and the wave kinetic equation that has been used in our previous studies [*Khazanov et al.*, 2002, 2003] can be summarized as follows. In the present study (1) the case of multispecies ($e - H^+ - He^+ - O^+$) plasma is considered, (2) wave propagation and refraction are rigorously taken into account in a full wave kinetic equation, (3) there is no wave reflection from the ionosphere because the He^+-mode reflects from the surfaces of the $O^+ - He^+$ bi-ion hybrid frequency, and in the present study we neglect the tunnelling of waves across the corresponding stop zone (only a minor portion of the EMIC wave energy can tunnel across the reflection region for the adopted O^+ content in the thermal density model). At the same time, we should note that nonperfect wave reflection can easily be incorporated in equation (22) by calculating the corresponding reflection coefficients using the results of Appendix B.

[35] In order to demonstrate the effects of EMIC wave propagation and refraction on the wave energy distributions and evolution, we have simulated the May 1998 storm and have presented the results for two time intervals during the storm. The first interval takes place on 2 May, from 24 hours to 48 hours after 1 May, 0000 UT, and covers the period of first *Dst* dip. The second one from 72 hours to 86 hours after 1 May, 0000 UT represents the period of largest *Dst* decrease on 4 May. The main conclusions of our simulation can be summarized as follows.

[36] 1. The density gradient at the plasmapause counteracts refraction caused by the magnetic field gradient and curvature. As a result, the net refraction is suppressed, and the He^+-mode grows preferably at the plasmapause. This finding is in complete agreement with the results of *Horne and Thorne* [1993], and *B* field distributions presented in (MLT, L shell) plane are very well organized by the plasmapause location (see Figure 6).

[37] 2. Comparison of the obtained global EMIC wave distributions with the results from another RAM based global model [*Kozyra et al.*, 1997; *Jordanova et al.*, 1997, 2001] demonstrates some similarities. Nevertheless in comparison with our results presented in Figure 6, the wave activity derived from this previous model (see Figure 8) occupies more extended equatorial zones, and those zones, shown in Figure 8, do not demonstrate that the plasmapause density gradient has a major impact on the wave excitation during the modeled event. Overall, this version of RAM [*Kozyra et al.*, 1997; *Jordanova et al.*, 1997, 2001] produces the more extended and less intense equatorial wave distributions during the May 1998 storm period than found by our more complete treatment of RC-EMIC waves interaction.

[38] 3. The derived wave kinetic equation (22) takes into account the energy outflow from the region of small wave normal angles to $\theta_0 = \pi/2$ (see second term in the left-hand side of equation (22)). The EMIC wave growth rate maximizes for $\theta_0 = 0$ and electron Landau damping has a peak for θ_0 close to 90°. As a consequence, the resulting power density distribution over wave normal angle depends on the ratios between rates of wave growth (mostly in the region of small θ_0), Landau damping (mostly at large θ_0), and $\dot{\theta}_0/\theta_0$. Almost none of the He^+-mode energy distributions over wave normal angle are Gaussian distributions (see Figure 9), and most important is that EMIC wave energy can occupy not only the region of generation, i.e., the region of small θ_0, but the entire wave normal angle region and even the region near $\theta_0 = \pi/2$ only. The latter is extremely crucial for energy transfer to thermal plasmaspheric electrons by resonant Landau damping, and subsequent downward heat transport and excitation of stable auroral red arcs [*Cornwall et al.*, 1971].

Appendix A: Ray Tracing Code Verification

[39] In order to test and verify our ray tracing code, we set out to reproduce previously published results for EMIC wave propagation. (All these results have been obtained for a dipole magnetic field configuration, and the plasma models specified below). A ray tracing study of EMIC waves in a multicomponent thermal plasma was first presented by *Rauch and Roux* [1982]. Because their study was motivated by the GEOS 1 and 2 spacecraft observations [*Young et al.*, 1981], only the H^+ and He^+ ions have been included in the thermal plasma model. All plasma species are assumed to be cold, and for plasma density variation they have used a magnetic model, $n_e \sim B$, with the constant He^+ abundance ratio of $\eta \equiv N_{He^+}/n_e = 0.2$. *Rauch and Roux* [1982] launched EMIC waves of classes *I*, *II*, and *III* at the equator at a geostationary distance where plasma density of $n_e = 40$ cm^{-3} has been assumed (see Figures 6, 7, and 8 in their paper). (Recall that the class *I* waves have frequencies below the He^+ ion gyrofrequency, and they are left-hand polarized. The class *II* waves have frequencies above the cutoff frequency, and they are left-hand and right-hand polarized below and above crossover frequency, respectively. The class *III* waves have frequencies from zero up to the H^+ ion gyrofrequency, and they are left-handed and right-handed above and below crossover frequency, respectively.) Using exactly the same setup in our ray tracing model as described above, we examined wave propagation for all three branches of EMIC waves, but only the results for class *III* are shown in Figure A1 (our raypath results for classes *I* and *II* are the same as in Figures 6 and 7 by *Rauch and Roux* [1982]). Raypath, wave normal angle, L shell, and latitude for EMIC waves of class *III* propagating in an $e - H^+ - He^+$ thermal plasma are presented in Figure A1. For $\eta = 0.2$, the crossover frequency $X_{cr} = 0.5$, and the bi-ion hybrid frequency $X_{bi} = 0.34$, we launch the left-hand polarized wave ray with $X = 0.55$ at the equator. This class of waves is well guided by the geomagnetic field and propagates toward the region of increased magnetic field. These waves suffer polarization reversal at point $X = X_{cr}$, and they are reflected at the point where X is slightly less than X_{bi}. As seen from Figure A1, the ray goes back and forth between the surfaces of the bi-ion hybrid frequency in opposite hemispheres, and radial drift of the ray is very small during these multiple bounces. Both the raypath and wave normal angle variation drawn in Figure A1 are very close to the results presented by

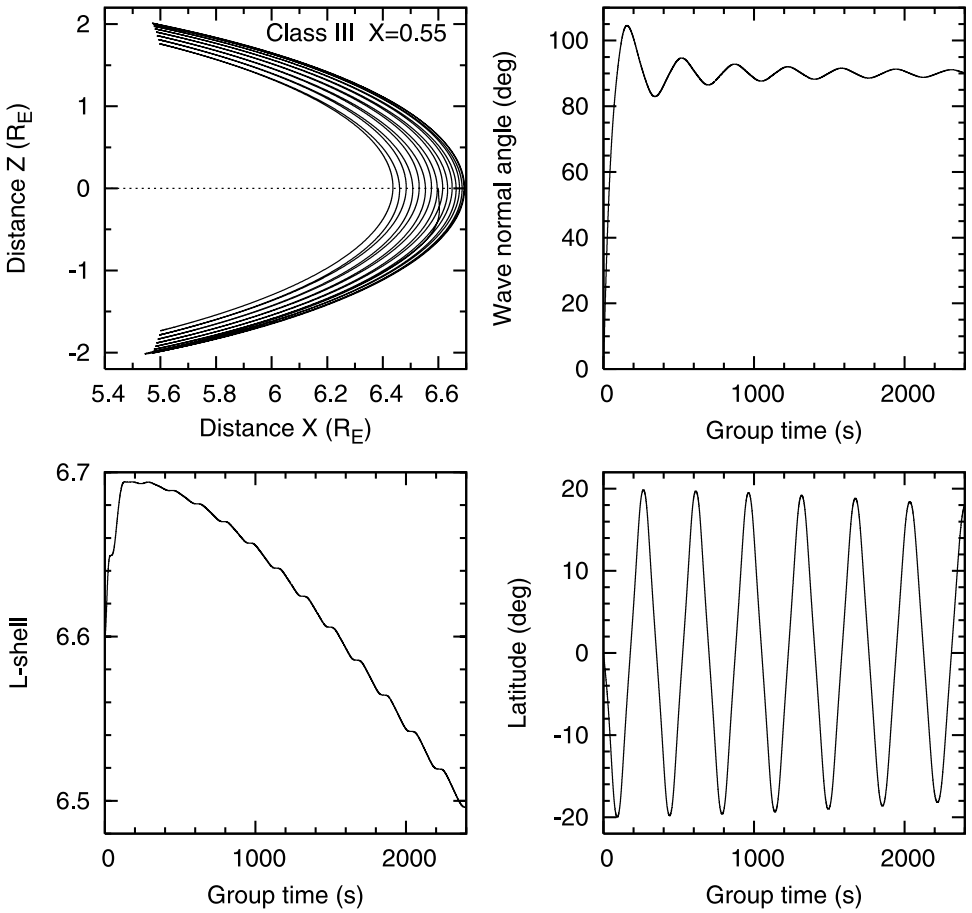

Figure A1. Raypath, wave normal angle, L shell, and latitude for EMIC waves of class *III* propagating in $e - H^+ - He^+$ thermal plasma are shown. A magnetic model, $n_e \sim B$ ($n_e = 40$ cm^{-3} at the equator), for plasma density with the constant He^+ abundance ratio of $\eta = 0.2$ is employed. Ray starts at the equator with $X \equiv \omega/\Omega_{H^+} = 0.55$, $\theta = 180$ deg, and the wave is left-hand polarized (for $\eta = 0.2$ crossover frequency $X_{cr} = 0.5$, and bi-ion hybrid frequency $X_{bi} = 0.34$).

Rauch and Roux [1982] in their Figures 8 and 9, and these comparisons can be considered successful.

[40] EMIC wave propagation in a more complicated medium has been modeled by *Horne and Thorne* [1993]. In this study not only have H^+ and He^+ ions have been included in the thermal plasma model, but also O^+ ions. *Horne and Thorne* [1993] employed much more realistic distributions for thermal plasma densities, namely, an analytical density model which includes the product of three terms: (1) diffusive equilibrium model term [*Angerami and Thomas*, 1964], (2) lower ionosphere factor, and (3) plasmapause and outer magnetosphere term. This model provides 2-D (MLT-independent) spatial distributions for electrons and H^+, He^+, O^+ ion species. (For more details about this density model see, e.g., *Angerami and Thomas* [1964], *Kimura* [1966], *Burtis* [1973], and *Inan and Bell* [1977].) Although the ray tracing program "HOTRAY" has been written for a hot plasma [*Horne*, 1989], all the raypaths presented by *Horne and Thorne* [1993] have been calculated for the cold plasma approximation. We next use the above thermal plasma model with exactly the same model setup as stated by *Horne and Thorne* [1993], and we calculate raypaths for all EMIC wave modes in such a plasma. Note, we identify these modes as O^+, He^+, H^+, and e modes [see *Khazanov et al.*, 2003, Figure 2] that corresponds to modes 6, 5, 4, and 3, respectively, in the work of *Horne and Thorne* [1993, Figure 2].

[41] In Figure A2 we present the ray phase path generated by our code for the initial conditions stated in Figure 7 of *Horne and Thorne* [1993]. We launch a left-hand polarized O^+-mode from the equator with $\omega/\Omega_{O^+} = 0.45$ and $\theta = 0$. Both the raypath and the wave normal angle variation agree well with the results obtained by *Horne and Thorne* [1993].

[42] Let us now compare the propagation characteristics of the He^+-mode in the frequency range $\Omega_{O^+} < \omega < \Omega_{He^+}$. The phase trajectories for this EMIC wave mode with the initial conditions from Figures 8, 9, and 10 in the paper [*Horne and Thorne*, 1993] are presented in Figures A3, A4, and A5, respectively. Figure A3 shows the results for a ray launched in the left-hand polarized mode from the geomagnetic equator at L = 3 with $\theta = 0$, and $\omega/\Omega_{O^+} = 2.4$. As one can see in this plot, the ray bounces between reflection points, and essentially stays on the same magnetic field line. In this case the wave normal angle rapidly increases due to dominance of the magnetic field gradient and curvature over the density gradient. Figure A4 demonstrates the results for

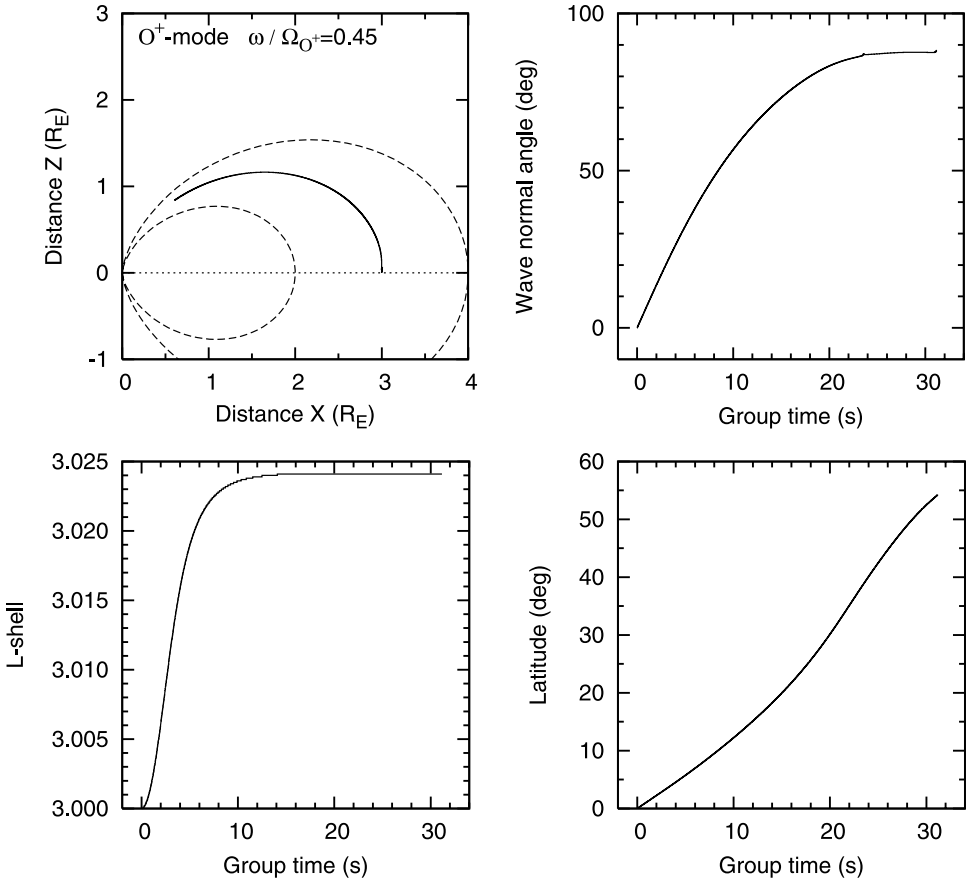

Figure A2. Raypath, wave normal angle, L shell, and latitude for O^+-mode propagating in $e - H^+ - He^+ - O^+$ thermal plasma are shown. The density model is the same as in the work of *Horne and Thorne* [1993]. The ray is launched from the equator with $\omega/\Omega_{O^+} = 0.45$, $\theta = 0$, and the wave is left-hand polarized.

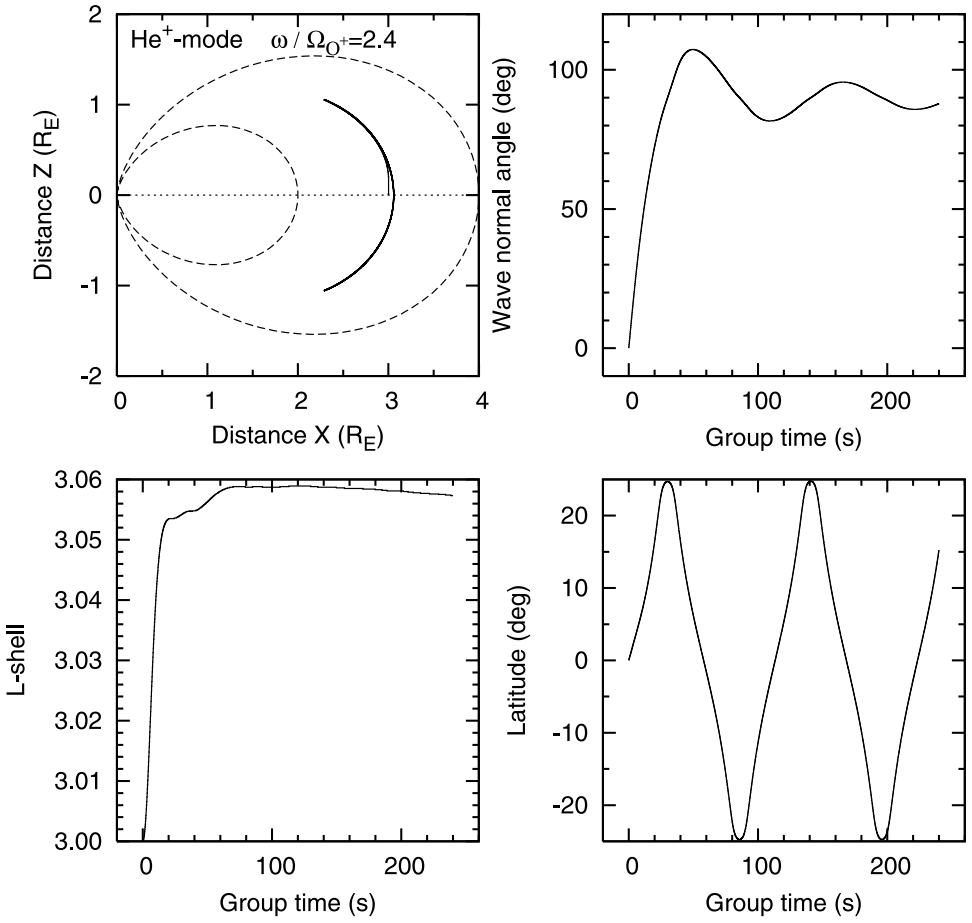

Figure A3. Same as Figure A2, except for He^{+}-mode with $\omega/\Omega_{O^{+}} = 2.4$.

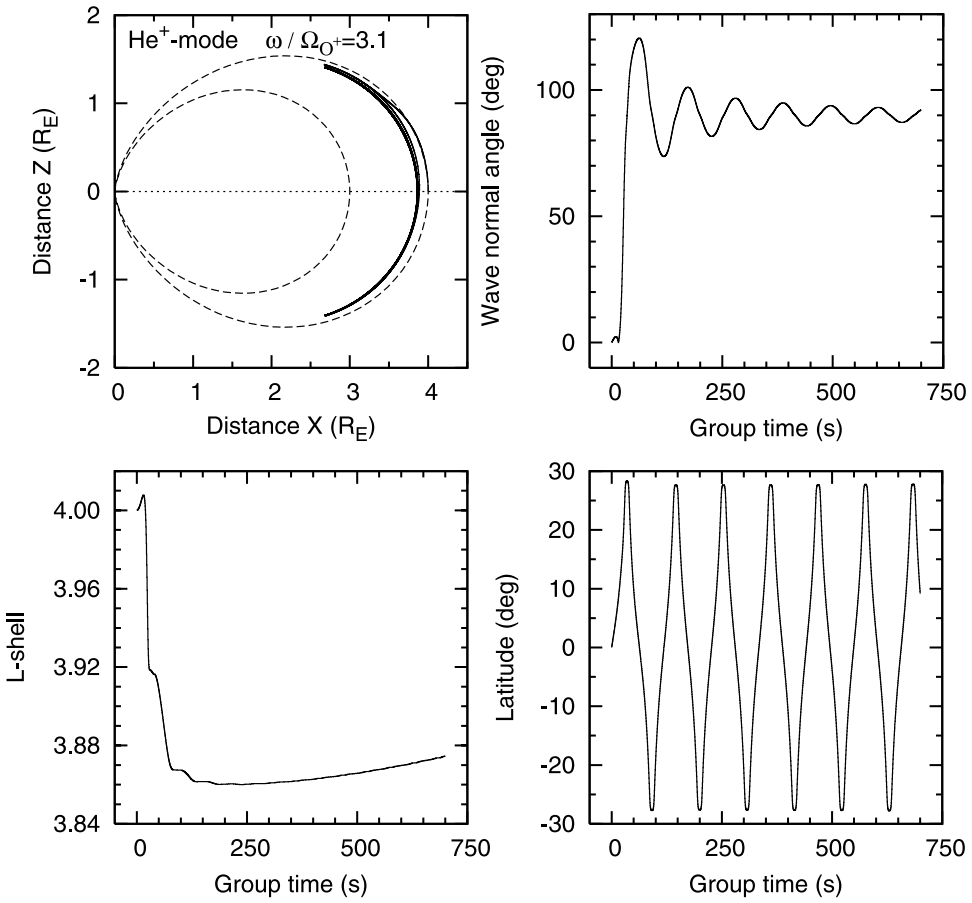

Figure A4. Same as Figure A3, except the ray is launched from L = 4 with $\omega/\Omega_{O^+} = 3.1$.

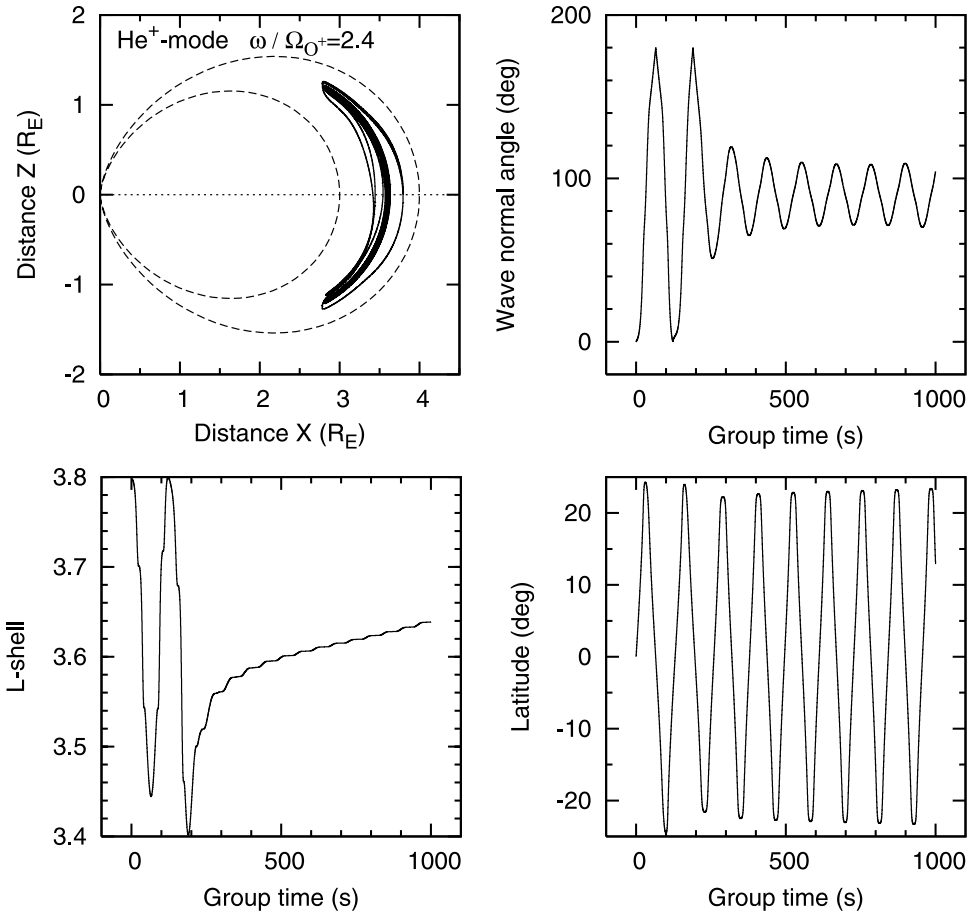

Figure A5. Same as Figure A3, except the ray is launched from L = 3.8 with $\omega/\Omega_{O^+} = 2.4$.

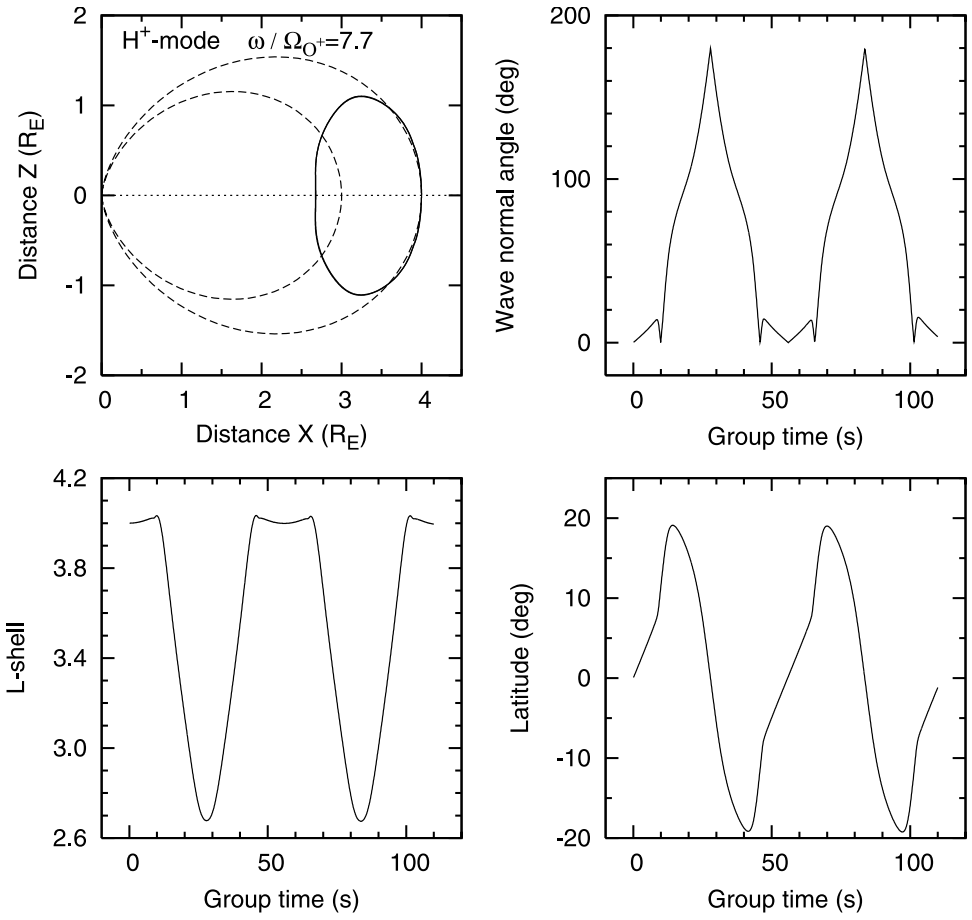

Figure A6. Same as Figure A4, except for the H^+-mode with $\omega/\Omega_{O^+} = 7.7$.

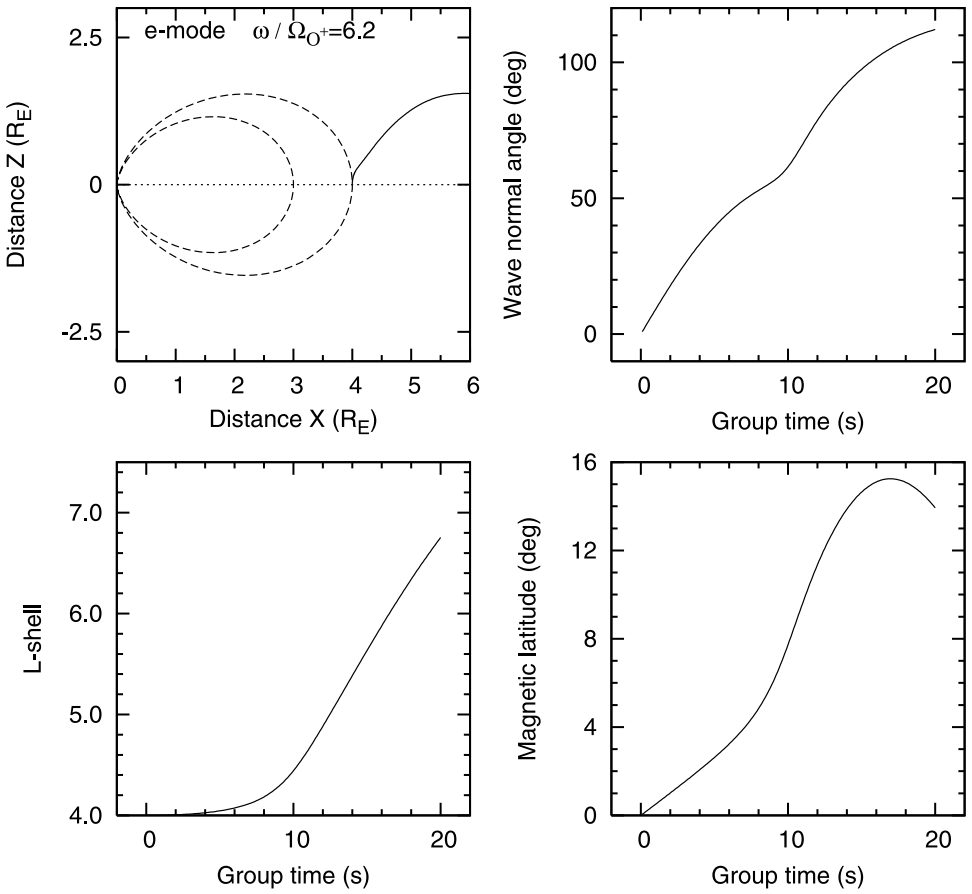

Figure A7. Same as Figure A6, except for the *e*-mode with $\omega/\Omega_{O^+} = 6.2$.

the left-hand polarized mode launched outside the plasmapause at L = 4 with $\theta = 0$, and $\omega/\Omega_{O^+} = 3.1$. The effect of the steep plasmapause density gradient on ray propagation is presented in Figure A5. We launch the left-hand polarized mode from the geomagnetic equator at L = 3.8 with $\theta = 0$, and $\omega/\Omega_{O^+} = 2.4$. In agreement with the results of *Horne and Thorne* [1993], after the first reflection the ray moves inward toward the Earth and crosses the equator at L = 3.4 with $\theta \simeq 180$ deg. Later, after reflection in the southern hemisphere, the ray returns to the equator at L = 3.8 and $\theta \simeq 0$. As we can see, the presented results well reproduce the results of *Horne and Thorne* [1993], except for slight differences between our Figure A5 and their Figure 10. In this connection, we found that the ray phase path in Figure A5 is very sensitive to the initial conditions if the ray is launched near L = 3.8, and we believe that the observed differences are due to slightly different constants used to setup the density model.

[43] Finally, in the frequency range $\Omega_{He^+} < \omega < \Omega_{H^+}$, our results that correspond to the initial conditions in Figures 12 and 11 by *Horne and Thorne* [1993], are shown in Figures A6 and A7, respectively. The H^+-mode with the left-hand polarization is launched from the equator at L = 4 with $\theta = 0$, $\omega/\Omega_{O^+} = 7.7$, and the results are presented in Figure A6. In this case the wave ray crosses the equator inside the plasmapause near L = 2.7 and outside the plasmapause near L = 4. All the ray characteristics change almost periodically. The left-hand polarized *e*-mode is launched at L = 4 with $\theta = 0$, and $\omega/\Omega_{O^+} = 6.2$. This mode is unguided and all the results are presented in Figure A7. As above, we again find good agreement with previous results with only slight differences between our Figure A6 and *Horne and Thorne* [1993, Figure 12] (see the above remark for the reason for these differences).

[44] Above is presented an extensive side by side comparison of our results with the previous ray tracing studies for different density models, and for all possible EMIC wave modes. Overall, we find very good agreement between the results, and we believe that our ray tracing code is validated.

Appendix B: Tunneling of EMIC Waves Across Reflection Region in Multi-Ion Magnetosphere

[45] In order to obtain the wave equation that describes EMIC wave propagation in the vicinity of the reflection point, we follow *Perraut et al.* [1984] and/or *Rauch and Roux* [1982]. Using the cold plasma approximation, we can present the dispersion equation in the vicinity of the reflection point as $k^2_{\|} + \Phi(z) = 0$, where $k_{\|}$ is a component of the wave vector parallel to the external magnetic field, z is a coordinate along the geomagnetic field line, and function $\Phi(z)$ can be found in the work of *Perraut et al.* [1984] and *Rauch and Roux* [1982]. This dispersion equation is obtained from Maxwell's equations after Fourier analysis. So the correct wave equation near the reflection point can easily be obtained by substituting

operator $-\partial^2/\partial z^2$ in the above dispersion equation instead of $k_\parallel^2$. This substitution leads to the following equation:

$$\frac{\partial^2 E(z)}{\partial z^2} - \Phi(z)E = 0, \tag{B1}$$

where E is a transverse electric field of EMIC waves. The component of the wave vector parallel to the external magnetic field should vanish at the reflection point, z_1, i.e., $\Phi(z_1) = 0$. So in the vicinity of this point we can present $\Phi(z)$ in the form:

$$\begin{aligned}\Phi(z) &\approx (z - z_1)\Phi'(z_1) \\ &= (z - z_1)\frac{\omega^2}{c^2}\left(-\frac{\partial S}{\partial z}\right)_{z_1}.\end{aligned} \tag{B2}$$

In equation (B2), c is the speed of light, function S will be specified below, and we took into account the fact that z_1 is very close to the point where the wave frequency is equal to the $O^+ - He^+$ bi-ion hybrid frequency, i.e., $S(z_1) \approx 0$. It follows from (B2) that a linear combination of the Airy functions is a solution for equation (B1) [see, e.g., *Abramowitz and Stegun*, 1964]. Taking into account that the wave electric field, E, should evanesce for $z > z_1$, we can write down the particular solution as

$$E(z) = \mathrm{Ai}\Big((z - z_1)(\Phi'(z_1))^{1/3}\Big), \tag{B3}$$

and easily obtain the transmission coefficient for wave amplitude, T. At a distance $\delta z = z_2 - z_1 > 0$ this coefficient is

$$T = \frac{E(z_2)}{E(z_1)}. \tag{B4}$$

Note that the wave power transmission factor is just T^2 in the case of adiabatic variance for plasma parameters.

[46] As we stated above, coordinate z_1 can be found from the following equation:

$$\begin{aligned}\omega^2 = \omega_{bi}^2(z_1) = {} & \frac{\Omega_p^2(z_1)}{256(\eta_1 + 0.25\eta_2 + 0.0625\eta_3)} \\ & \times \left(\eta_1 + 0.25\eta_2 + \eta_3 + \frac{15\eta_1\eta_3}{\eta_1 + 4.25\eta_2 + \eta_3}\right),\end{aligned} \tag{B5}$$

where ω_{bi} is the $O^+ - He^+$ bi-ion hybrid frequency, Ω_p is a local proton gyrofrequency, and η_1, η_2, η_3 ($\eta_1 + \eta_2 + \eta_3 = 1$) are the relative densities for plasmaspheric H^+, He^+, and O^+ ions, respectively. In order to find coordinate z_2, we follow *Perraut et al.* [1984] and use equation:

$$\omega = \Omega_{O^+}(z_2), \tag{B6}$$

where Ω_{O^+} is an oxygen gyrofrequency. Further, for the cold plasma approximation, function S introduced in equation (B2) has the form of

$$S = -\frac{\omega_{pe}^2}{(|\Omega_e|\Omega_p}\left(\frac{\eta_1}{y^2 - 1} + \frac{4\eta_2}{(4y)^2 - 1} + \frac{16\eta_3}{(16y)^2 - 1}\right), \tag{B7}$$

where ${\omega_{pe}}^2 = 4\pi\, n_e e^2/m_e$ is the squared electron plasma frequency, $\Omega_e = eB/m_e c$ is a local electron gyrofrequency, and $y = \omega/\Omega_p$ is the normalized wave frequency.

[47] For simplicity, we use a magnetic model, $n_e \sim B$, for the cold plasma density, consider η_1, η_2, η_3 to be coordinate independent, and use parabolic approximation for the geomagnetic field B near the equator,

$$B(z) = B(0)\left(1 + \frac{z^2}{z_0^2}\right), \quad z_0 = \frac{\sqrt{2}}{3}r_0, \tag{B8}$$

where r_0 is the radial distance in the magnetic equatorial plane. These assumptions allow us to easily calculate the derivative in equation (B2) which takes the form of

$$\begin{aligned}\left(-\frac{\partial S}{\partial z}\right)_{z_1} = {} & \left(\frac{\omega_{pe}^2}{|\Omega_e|\Omega_p}\right)_{z_1}\frac{2z_1}{(z_0^2 + z_1^2)} \\ & \times \left(\eta_1\frac{y^2 + 1}{(y^2 - 1)^2} + 4\eta_2\frac{(4y)^2 + 1}{\Big((4y)^2 - 1\Big)^2}\right. \\ & \left. + 16\eta_3\frac{(16y)^2 + 1}{\Big((16y)^2 - 1\Big)^2}\right)_{z_1}.\end{aligned} \tag{B9}$$

[48] **Acknowledgments.** We thank the two referees for their constructive and detailed comments. GVK thanks B. J. Fraser and R. M. Thorne for useful, stimulating discussions. Funding in support of this study was provided by NASA grant UPN 370-16-10. This research was performed while K. Gamayunov held a NASA Postdoctoral Program appointment at NASA/MSFC. Support for D. Gallagher is provided by the IMAGE Mission through the NASA Science Mission Directorate.

References

Abramowitz, M., and I. A. Stegun (1964), *Handbook of Mathematical Functions*, Natl. Bur. of Stand., Washington, D. C.

Akhiezer, A. I., I. A. Akhiezer, R. V. Polovin, A. G. Sitenko, and K. N. Stepanov (1975), *Plasma Electrodynamics*, vol. 2, Elsevier, New York.

Anderson, B. J., R. E. Erlandson, and L. J. Zanetti (1992a), A statistical study of Pc 1-2 magnetic pulsations in the equatorial magnetosphere, 1, Equatorial occurrence distributions, *J. Geophys. Res.*, *97*, 3075.

Anderson, B. J., R. E. Erlandson, and L. J. Zanetti (1992b), A statistical study of Pc 1-2 magnetic pulsations in the equatorial magnetosphere, 2, Wave properties, *J. Geophys. Res.*, *97*, 3089.

Angerami, J. J., and J. O. Thomas (1964), Studies of planetary atmospheres, 1, The distribution of ions and electrons in the Earth's exosphere, *J. Geophys. Res.*, *69*, 4537.

Bespalov, P. A., and V. Y. Trakhtengerts (1986), Cyclotron instability of the Earth radiation belts, in *Reviews of Plasma Physics*, vol. 10, edited by M. A. Leontovich, pp. 155–192, Springer, New York.

Bezrukikh, V. V., and K. I. Gringauz (1976), The hot zone in the outer plasmasphere of the Earth, *J. Atmos. Terr. Phys.*, *38*, 1085.

Bräysy, T., K. Mursula, and G. Marklund (1998), Ion cyclotron waves during a great magnetic storm observed by Freja double-probe electric field instrument, *J. Geophys. Res.*, *103*, 4145.

Burtis, W. J. (1973), User's guide to the Stanford VLF raytracing program, report, Space, Telecom. and Radiosci. Lab., Stanford Univ., Stanford, Calif.

Chamberlain, J. W. (1963), Planetary corona and atmospheric evaporation, *Planet. Space Sci.*, *11*, 901.

Cornwall, J. M. (1964), Cyclotron instabilities and electromagnetic emission generation mechanisms, *J. Geophys. Res.*, *69*, 4515.

Cornwall, J. M. (1965), Cyclotron instabilities and electromagnetic emission in the ultra low frequency and very low frequency ranges, *J. Geophys. Res.*, *70*, 61.

Cornwall, J. M., F. V. Coroniti, and R. M. Thorne (1970), Turbulent loss of ring current protons, *J. Geophys. Res.*, *75*, 4699.

Cornwall, J. M., F. V. Coroniti, and R. M. Thorne (1971), Unified theory of SAR arc formation at the plasmapause, *J. Geophys. Res.*, *76*, 4428.

Denton, R. E., M. K. Hudson, and I. Roth (1992), Loss-cone-driven ion cyclotron waves in the magnetosphere, *J. Geophys. Res.*, *97*, 12,093.

Ebihara, Y., and M. Ejiri (2000), Simulation study on fundamental properties of the storm-time ring current, *J. Geophys. Res.*, *105*, 15,843.

Ebihara, Y., M.-C. Fok, R. A. Wolf, T. J. Immel, and T. E. Moore (2004), Influence of ionospheric conductivity on the ring current, *J. Geophys. Res.*, *109*, A08205, doi:10.1029/2003JA010351.

Ebihara, Y., M.-C. Fok, R. A. Wolf, M. F. Thomsen, and T. E. Moore (2005), Nonlinear impact of plasma sheet density on the storm-time ring current, *J. Geophys. Res.*, *110*, A02208, doi:10.1029/2004JA010435.

Engebretson, M. J., et al. (2005), Pc-1 waves and associated unstable distributions of magnetospheric protons during three extended conjunctions between the polar satellite and Antarctic ground stations, paper presented at IAGA meeting, Toulouse, France, 25 July.

Engebretson, A. Keiling, K.-H. Fornacon, C. A. Cattell, J. R. Johnson, J. L. Posch, S. R. Quick, K.-H. Glassmeier, G. K. Parks, and H. Réme, (2006), Cluster observations of Pc 1–2 waves and associated ion distributions during the October and November 2003 magnetic storms, *Planet. Space Sci.*, in press.

Erlandson, R. E., and A. J. Ukhorskiy (2001), Observations of electromagnetic ion cyclotron waves during geomagnetic storms: Wave occurrence and pitch angle scattering, *J. Geophys. Res.*, *106*, 3883.

Erlandson, R. E., L. J. Zanetti, T. A. Potemra, L. P. Block, and G. Holmgren (1990), Viking magnetic and electric field observations of Pc 1 waves at high latitudes, *J. Geophys. Res.*, *95*, 5941.

Farrugia, C. J., et al. (2003), Large-scale geomagnetic effects of May 4, 1998, *Adv. Space Res.*, *31*(4), 1111.

Fok, M.-C., J. U. Kozyra, A. F. Nagy, C. E. Rasmussen, and G. V. Khazanov (1993), A decay model of equatorial ring current and the associated aeronomical consequences, *J. Geophys. Res.*, *98*, 19,381.

Fok, M.-C., et al. (2003), Global ENA image simulations, *Space Sci. Rev.*, *109*, 77.

Galeev, A. A. (1975), Plasma turbulence in the magnetosphere with special regard to plasma heating, in *Physics of the Hot Plasma in the Magnetosphere*, edited by B. Hultquist and L. Stenflo, p. 251, Springer, New York.

Garcia, H. A., and W. N. Spjeldvik (1985), Anisotropy characteristics of geomagnetically trapped ions, *J. Geophys. Res.*, *90*, 347.

Gendrin, R., M. Ashour-Abdalla, Y. Omura, and K. Quest (1984), Linear analysis of ion-cyclotron interaction in a multicomponent plasma, *J. Geophys. Res.*, *89*, 9119.

Gomberoff, L., and R. Neira (1983), Convective growth rate of ion cyclotron waves in a $H^+ - He^+$ and $H^+ - He^+ - O^+$ plasma, *J. Geophys. Res.*, *88*, 2170.

Gonzalez, W. D., B. T. Tsurutani, A. L. C. Gonzalez, E. J. Smith, F. Tang, and S.-I. Akasofu (1989), Solar wind-magnetosphere coupling during intense magnetic storms (1978–1979), *J. Geophys. Res.*, *94*, 8835.

Gorbachev, O. A., G. V. Khazanov, K. V. Gamayunov, and E. N. Krivorutsky (1992), A theoretical model for the ring current interaction with the Earth's plasmasphere, *Planet. Space Sci.*, *40*, 859.

Gringauz, K. I. (1983), Plasmasphere and its interaction with ring current, *Space Sci. Rev.*, *34*, 245.

Gringauz, K. I. (1985), Structure and properties of the Earth plasmasphere, *Adv. Space Res.*, *5*(4), 391.

Haselgrove, C. B., and J. Haselgrove (1960), Twisted ray paths in the ionosphere, *Proc. Phys. Soc.*, *75*, 357.

Haselgrove, J. (1954), Ray theory and a new method for ray tracing, *Report of Conference on the Physics of the Ionosphere*, p. 355, Phys. Soc., London.

Horne, R. B. (1989), Path-integrated growth of electrostatic waves: The generation of terrestrial myriametric radiation, *J. Geophys. Res.*, *94*, 8895.

Horne, R. B., and R. M. Thorne (1993), On the preferred source location for the convective amplification of ion cyclotron waves, *J. Geophys. Res.*, *98*, 9233.

Horwitz, J. L., C. R. Baugher, C. R. Chappell, E. G. Shelley, D. T. Young, and R. R. Anderson (1981), ISEE 1 observations of thermal plasma during periods of quieting magnetic activity, *J. Geophys. Res.*, *86*, 9989.

Inan, U. S., and T. F. Bell (1977), The plasmapause as a VLF wave guide, *J. Geophys. Res.*, *82*, 2819.

Iyemori, T., and K. Hayashi (1989), Pc 1 micropulsations observed by Magsat in ionospheric F region, *J. Geophys. Res.*, *94*, 93.

Jordanova, V. K., J. U. Kozyra, G. V. Khazanov, A. F. Nagy, C. E. Rasmussen, and M.-C. Fok (1994), A bounce-averaged kinetic model of the ring current ion population, *Geophys. Res. Lett.*, *21*, 2785.

Jordanova, V. K., L. M. Kistler, J. U. Kozyra, G. V. Khazanov, and A. F. Nagy (1996a), Collisional losses of ring current ions, *J. Geophys. Res.*, *101*, 111.

Jordanova, V. K., J. U. Kozyra, and A. F. Nagy (1996b), Effects of heavy ions on the quasi-linear diffusion coefficients from resonant interactions with EMIC waves, *J. Geophys. Res.*, *101*, 19,771.

Jordanova, V. K., J. U. Kozyra, A. F. Nagy, and G. V. Khazanov (1997), Kinetic model of the ring current-atmosphere interactions, *J. Geophys. Res.*, *102*, 14,279.

Jordanova, V. K., C. J. Farrugia, L. Janoo, J. M. Quinn, R. B. Torbert, K. W. Ogilvie, R. P. Lepping, J. T. Steinberg, D. J. McComas, and R. D. Belian (1998a), October 1995 magnetic cloud and accompanying storm activity: Ring current evolution, *J. Geophys. Res.*, *103*, 79.

Jordanova, V. K., C. J. Farrugia, J. M. Quinn, R. M. Thorne, K. W. Ogilvie, R. P. Lepping, G. Lu, A. J. Lazarus, M. F. Thomsen, and R. D. Belian (1998b), Effect of wave-particle interactions on ring current evolution for January 10–11, 1997: Initial results, *Geophys. Res. Lett.*, *25*, 2971.

Jordanova, V. K., C. J. Farrugia, R. M. Thorne, G. V. Khazanov, G. D. Reeves, and M. F. Thomsen (2001), Modeling ring current proton precipitation by EMIC waves during the May 14–16, 1997, storm, *J. Geophys. Res.*, *106*, 7.

Jordanova, V. K., A. Boonsiriseth, R. M. Thorne, and Y. Dotan (2003), Ring current asymmetry from global simulations using a high-resolution electric field model, *J. Geophys. Res.*, *108*(A12), 1443, doi:10.1029/2003JA009993.

Kennel, C. F., and H. E. Petschek (1966), Limit on stably trapped particle fluxes, *J. Geophys. Res.*, *71*, 1.

Khazanov, G. V., K. V. Gamayunov, V. K. Jordanova, and E. N. Krivorutsky (2002), A self-consistent model of the interacting ring current ions and electromagnetic ion cyclotron waves, initial results: Waves and precipitating fluxes, *J. Geophys. Res.*, *107*(A6), 1085, doi:10.1029/2001JA000180.

Khazanov, G. V., K. V. Gamayunov, and V. K. Jordanova (2003), Self-consistent model of magnetospheric ring current ions and electromagnetic ion cyclotron waves: The 2–7 May 1998 storm, *J. Geophys. Res.*, *108*(A12), 1419, doi:10.1029/2003JA009856.

Kimura, I. (1966), Effects of ions on whistler-mode ray tracing, *Radio Sci.*, *1*, 269.

Kozyra, J. U., T. E. Cravens, A. F. Nagy, E. G. Fontheim, and R. S. B. Ong (1984), Effects of energetic heavy ions on electromagnetic ion cyclotron wave generation in the plasmapause region, *J. Geophys. Res.*, *89*, 2217.

Kozyra, J. U., V. K. Jordanova, R. B. Horne, and R. M. Thorne (1997), Modeling of the contribution of Electromagnetic Ion Cyclotron (EMIC) waves to stromtime ring current erosion, in *Magnetic Storms*, *Geophys. Monogr. Ser.*, vol. 98, edited by B. T. Tsurutani et al., p. 187, AGU, Washington, D. C.

Kozyra, J. U., M. W. Liemohn, C. R. Clauer, A. J. Ridley, M. F. Thomsen, J. E. Borovsky, J. L. Roeder, and V. K. Jordanova (2002), Two-step Dst development and ring current composition changes during the 4–6 June 1991 magnetic storm, *J. Geophys. Res.*, *107*(A8), 1224, doi:10.1029/2001JA000023.

LaBelle, J., R. A. Treumann, W. Baumjohann, G. Haerendel, N. Sckopke, G. Paschmann, and H. Lühr (1988), The duskside plasmapause/ring current interface: Convection and plasma wave observations, *J. Geophys. Res.*, *93*, 2573.

Liemohn, M. W., A. J. Ridley, D. L. Gallagher, D. M. Ober, and J. U. Kozyra 2004, Dependence of plasmaspheric morphology on the electric field description during the recovery phase of the April 17, 2002 magnetic storm, *J. Geophys. Res.*, *109*, A03209, doi:10.1029/2003JA010304.

Loto'aniu, T. M., B. J. Fraser, and C. L. Waters (2005), Propagation of electromagnetic ion cyclotron wave energy in the magnetosphere, *J. Geophys. Res.*, *110*, A07214, doi:10.1029/2004JA010816.

Lyons, L. R. (1974), Pitch angle and energy diffusion coefficients from resonant interactions with ion-cyclotron and whistler waves, *J. Plasma Phys.*, *12*, 417.

Lyons, L. R., and D. J. Williams (1984), *Quantitative Aspects of Magnetospheric Physics*, Springer, New York.
Mauk, B. H. (1982), Helium resonance and dispersion effects on geostationary Alfvén/ion cyclotron waves, *J. Geophys. Res.*, *87*, 9107.
Perraut, S., R. Gendrin, A. Roux, and C. de Villedary (1984), Ion cyclotron waves: Direct comparison between ground-based measurements and observations in the source region, *J. Geophys. Res.*, *89*, 195.
Rairden, R. L., L. A. Frank, and J. D. Craven (1986), Geocoronal imaging with Dynamics Explorer, *J. Geophys. Res.*, *91*, 13,613.
Rasmussen, C. E., S. M. Guiter, and S. G. Thomas (1993), Two-dimensional model of the plasmasphere: Refilling time constants, *Planet. Space Sci.*, *41*, 35.
Rauch, J. L., and A. Roux (1982), Ray tracing of ULF waves in a multicomponent magnetospheric plasma: Consequences for the general mechanism of ion cyclotron waves, *J. Geophys. Res.*, *87*, 8191.
Roux, A., S. Perraut, J. L. Rouch, C. de Villedary, G. Kremser, A. Korth, and D. T. Young (1982), Wave-particle interactions near Ω_{He+} observed on board GEOS 1 and 2, 2, Generation of ion cyclotron waves and heating of He^+ ions, *J. Geophys. Res.*, *87*, 8174.
Sheldon, R. B., and D. C. Hamilton (1993), Ion transport and loss in the Earth's quiet ring current, 1, Data and standard model, *J. Geophys. Res.*, *98*, 13,491.
Stern, D. P. (1975), The motion of a proton in the equatorial magnetosphere, *J. Geophys. Res.*, *80*, 595.
Stix, T. H. (1992), *Waves in Plasmas*, Am. Inst. of Phys., College Park, Md.
Summers, D., and R. M. Thorne (2003), Relativistic electron pitch-angle scattering by electromagnetic ion cyclotron waves during geomagnetic storms, *J. Geophys. Res.*, *108*(A4), 1143, doi:10.1029/2002JA009489.
Volland, H. (1973), A semiempirical model of large-scale magnetospheric electric fields, *J. Geophys. Res.*, *78*, 171.
Walt, M., and H. D. Voss (2001), Losses of ring current ions by strong pitch angle scattering, *Geophys. Res. Lett.*, *28*, 3839.
Walt, M., and H. D. Voss (2004), Proton precipitation during magnetic storms in August through November 1998, *J. Geophys. Res.*, *108*, A02201, doi:10.1029/2003JA010083.
Yabroff, I. (1961), Computation of whistler ray paths, *Radio Sci.*, *65*, 485.
Young, D. T., T. J. Geiss, H. Balsiger, P. Eberhardt, A. Ghiedmetti, and H. Rosenbauer (1977), Discovery of He^{2+} and O^{2+} ions of terrestrial origin in the outer magnetosphere, *Geophys. Res. Lett.*, *4*, 561.
Young, D. T., S. Perraut, A. Roux, C. de Villedary, R. Gendrin, A. Korth, G. Kremser, and D. Jones (1981), Wave-particle interactions near Ω_{He^+} observed on GEOS 1 and 2, 1, Propagations of ion cyclotron waves in He^+-rich plasma, *J. Geophys. Res.*, *86*, 6755.

D. L. Gallagher, K. V. Gamayunov, and G. V. Khazanov, Space Science Department, National Space Science and Technology Center, NASA Marshall Space Flight Center, 320 Sparkman Drive, Huntsville, AL 35805, USA. (dennis.l.gallagher@nasa.gov; konstantin.gamayunov@msfc.nasa.gov; george.khazanov@msfc.nasa.gov)

J. U. Kozyra, Space Physics Research Laboratory, University of Michigan, 2455 Hayward Street, Ann Arbor, MI 49109, USA. (jukozyra@umich.edu)